

Using the topology of large-scale structure in the WiggleZ Dark Energy Survey as a cosmological standard ruler

Chris Blake^{1*}, J. Berian James^{2,3} and Gregory B. Poole⁴

¹ *Centre for Astrophysics & Supercomputing, Swinburne University of Technology, P.O. Box 218, Hawthorn, VIC 3122, Australia*

² *Astronomy Department, University of California, Berkeley, CA 94720-3411, USA*

³ *Dark Cosmology Centre, University of Copenhagen, Juliane Maries Vej 30, 2100 Copenhagen Ø, Denmark*

⁴ *School of Physics, University of Melbourne, Parkville, VIC 3010, Australia*

20 September 2018

ABSTRACT

We present new and accurate measurements of the cosmic distance-redshift relation, spanning $0.2 < z < 1$, using the topology of large-scale structure as a cosmological standard ruler. Our results derive from an analysis of the Minkowski functionals of the density field traced by the WiggleZ Dark Energy Survey. The Minkowski functionals are a set of statistics which completely describe the topological nature of each isodensity surface within the field, as a function of the density value. Given the shape of the underlying matter power spectrum, measured by fluctuations in the Cosmic Microwave Background radiation, the expected amplitudes of the Minkowski functionals are specified as an excursion set of a Gaussian random field, with minimal non-Gaussian corrections for the smoothing scales $\geq 10 h^{-1}$ Mpc considered in this analysis. The measured amplitudes then determine the cosmic distance $D_V(z)$, which we obtain with 3 – 7% accuracies in six independent redshift slices, with the standard ruler originating in the known curvature of the model power spectrum at the smoothing scale. We introduce a new method for correcting the topological statistics for the sparse-sampling of the density field by the galaxy tracers, and validate our overall methodology using mock catalogues from N-body simulations. Our distance measurements are consistent with standard models which describe the cosmic expansion history, and with previous analyses of baryon acoustic oscillations (BAOs) detected by the WiggleZ Survey, with the topological results yielding a higher distance precision by a factor of 2. However, the full redshift-space power-spectrum shape is required to recover the topological distances, in contrast to the preferred length scale imprinted by BAOs, which is determined by simpler physics.

Key words: surveys, large-scale structure of Universe, distance scale, galaxies: statistics

1 INTRODUCTION

The large-scale structure of the Universe, mapped by large galaxy surveys, is one of the principal tools for testing the physical laws on cosmological scales; in particular the unknown nature of the ‘dark energy’ which appears to dominate today’s Universe. The pattern of the galaxy distribution is sensitive to the matter and energy constituents of the Universe, the cosmic expansion history, and the gravitational physics which amplifies the initial density seeds into today’s web of structure. However, it is also affected by processes for which there currently exists no complete model:

the non-linear gravitational evolution of structure beyond perturbation theory, redshift-space distortions due to galaxy peculiar velocities, and galaxy bias, which describes the complex astrophysical manner in which the observed galaxy distribution traces the underlying mass. The major challenge for cosmological analyses of large-scale structure is to extract robust information about the underlying cosmological quantities in the presence of the poorly-modelled non-linear or astrophysical effects.

For example, one of the most important methods for obtaining robust cosmological information from large-scale structure surveys is to use the baryon acoustic oscillations (BAOs) encoded in the clustering pattern as a standard ruler to map out the cosmic expansion history (Eisenstein, Hu &

* E-mail: cblake@astro.swin.edu.au

Tegmark 1998, Blake & Glazebrook 2003, Seo & Eisenstein 2003). This technique exploits a preferred length scale imprinted in the clustering of galaxies, a late-time signature of the sound waves which propagated in the pre-recombination Universe (Peebles & Yu 1970, Sunyaev & Zeldovitch 1970, Hu & Sugiyama 1996). This preferred scale, accurately calibrated by measurements of the Cosmic Microwave Background (CMB) radiation, may be extracted from the galaxy survey observations in a manner which is independent of any other details of the clustering pattern (e.g., Anderson et al. 2012). This is an attractive approach because the general clustering pattern is subject to the non-linear and astrophysical distortions mentioned above (e.g. Eisenstein, Seo & White 2007, Smith, Scoccimarro & Sheth 2008, Seo et al. 2008), which may be harder to model. However, seen from another viewpoint, this ‘model-independent’ technique excludes information which may in principle be used to improve cosmological constraints. The BAO standard-ruler method has now been applied to a number of galaxy surveys to map out the cosmic expansion history across a wide range of redshifts (e.g. Eisenstein et al. 2005, Percival et al. 2010, Blake et al. 2011c, Beutler et al. 2011, Anderson et al. 2012, Busca et al. 2013).

The measurement of BAOs is an example of the use of 2-point clustering statistics, such as the correlation function or power spectrum, which are almost ubiquitous for testing cosmological models using galaxy surveys. However, the 2-point statistics do not describe all of the information contained in the cosmological density field. Lacking any sensitivity to the phases of the underlying density Fourier modes, they specifically filter out the direct morphological information which is most striking in any visual examination of the ‘cosmic web’: its filamentary nature of inter-connected voids, walls and nodes. Indeed, two completely different spatial patterns could display the same 2-point correlation function (e.g. Martinez et al. 1990). A more complete description of the information can make use of a hierarchy of correlation functions, but these are cumbersome to implement beyond the 3-point function, and modelling their non-linear evolution presents difficulties.

A less-studied but promising alternative approach for extracting information from large-scale structure surveys is to quantify the topological statistics of the cosmological density field. In this study we focus on the Minkowski functionals (Mecke, Buchert & Wagner 1994), a set of statistics supplied by integral geometry for the complete morphological specification of spatial patterns. The Minkowski functionals are computed from a density field, following smoothing by a Gaussian filter, by considering the topological nature of the surfaces formed by each isodensity threshold. In particular, for each surface, the four Minkowski functionals describe the volume enclosed, surface area, curvature and ‘connectivity’ (formally defined by either the Euler characteristic or genus statistic). We note that a number of alternative topological approaches exist for quantifying large-scale structure such as studies of cosmic voids (Lavaux & Wandelt 2012), wavelet analysis (Martinez, Paredes & Saar 1993), minimal spanning trees (Barrow, Bhavsar & Sonoda 1985), and multiscale morphology filters (Aragon-Calvo, van de Weygaert & Jones 2010).

Topological statistics are worth exploring as a test of cosmological models because they may be robust against

some of the systematic non-linear processes which are typically difficult to model in the correlation functions (Melott, Weinberg & Gott 1988, Matsubara 2003, Park & Kim 2010). In particular, any process which modifies the density field, preserving the rank-ordering of density from its initial state, will not affect the topology of isodensity contours enclosing a given fraction of volume (Gott, Melott & Dickinson 1986); nor does the continuous deformation of a structure affect its topological connectedness. As such, the Minkowski functionals are completely unaffected by linear structure growth and local, monotonic, non-linear galaxy bias. Moreover they are only very weakly distorted by non-linear gravitational evolution and redshift-space distortions (Matsubara 1994, Matsubara & Yokoyama 1996). In summary, the topology of the density field in co-moving space is exactly conserved over time during linear evolution, and non-linear corrections remain small for scales $\geq 10 h^{-1}$ Mpc. Indeed, we determine that the most important systematic modelling issue in our analysis is not non-linear evolution, but the ‘sparse-sampling’ distortions arising when the smoothing scale of the Gaussian filter is comparable to the mean inter-galaxy separation (James 2012). We also note that, even if the initial density statistics were significantly non-Gaussian, the topological statistics would nonetheless be conserved during linear evolution.

The pattern of matter overdensities today reflects the distribution of ‘seeds’ from which they were formed. If this initial distribution constituted a Gaussian random field as assumed in this study, predicted by simple models of inflation, and supported by observations of the CMB, then the Minkowski functionals of the smoothed density field have simple analytic forms. In this case the dependence of the functionals on the isodensity threshold ν is a known function of ν , regardless of the power spectrum of the field, with an unknown overall normalization that only depends on the shape of the underlying power spectrum at the smoothing scale. If the shape of this power spectrum is known, then theory predicts each of the Minkowski functionals, independently of the normalization of the underlying power spectrum.

A measurement of the Minkowski functional amplitudes is then sensitive to the cosmic distance-redshift relation in two ways, which allow a ‘standard ruler’ technique to be applied (Park & Kim 2010, Zunckel, Gott & Lunnan 2011). First, the distance-redshift relation determines the physical length-scales mapped by the survey, and hence the amplitudes of the Minkowski functionals in dimensional units. Secondly, the smoothing scale applied when filtering the density field in order to perform these measurements assumes a fiducial distance-redshift relation, and selects a scale in the underlying model power spectrum to which the measurements are sensitive. For a power-law power spectrum these two effects are precisely degenerate, yielding no sensitivity of the Minkowski functional amplitudes to the distance scale. However, if the underlying power spectrum possesses a curvature which is accurately known, for example using models fit to CMB observations, then this curvature may be used as a standard ruler to match the smoothing scale which has been applied to the data. For a narrow redshift slice z of a galaxy survey, the resulting observable is the ‘volume-weighted’ distance $D_V(z)$, identical to the quantity measured by BAO surveys using the angle-averaged correlation function.

The aim of our study is to measure these topological statistics using data from the WiggleZ Dark Energy Survey (Drinkwater et al. 2010), which is one of the largest existing large-scale structure surveys, and provides a uniquely-long redshift baseline ($0.2 < z < 1$) for testing the cosmological model. We use the Minkowski functional amplitudes to measure the distance-redshift relation $D_V(z)$ and compare the result to analyses using BAOs (Blake et al. 2011c), validating our techniques using mock galaxy catalogues from N-body simulations. In comparison to previous analyses which have focused on measuring just one of the Minkowski functionals, the genus statistic, from the Sloan Digital Sky Survey (Gott et al. 2009, Choi et al. 2010) or from large N-body simulations (Kim et al. 2011), we implement some new methodological developments: (1) we apply a new method of estimating the galaxy density field correcting for the survey selection function; (2) we measure and utilize all Minkowski functionals rather than just the genus statistic; (3) we advocate and apply a study of the *differential* Minkowski functionals rather than the integral versions, in order to reduce covariance between measurements at different values of ν ; (4) we measure this covariance between different density thresholds and functionals, and propagate this information into our cosmological fits; (5) we prescribe a method for correcting our measurements for sparse-sampling.

Our paper is structured as follows: in section 2 we describe the various datasets employed in our analysis, including the WiggleZ galaxy survey and mock catalogues. In section 3 we present the Minkowski functional measurements and modelling. In section 4 we extract the Minkowski functional amplitudes and their covariances, to which we fit cosmological models in section 5. We present our conclusions in section 6.

2 DATA

2.1 The WiggleZ Dark Energy Survey

The WiggleZ Dark Energy Survey (Drinkwater et al. 2010) is a large-scale galaxy redshift survey of bright emission-line galaxies over the redshift range $z < 1$, which was carried out at the Anglo-Australian Telescope between August 2006 and January 2011. In total, of order 200,000 redshifts of UV-selected galaxies were obtained, covering of order 1000 deg² of equatorial sky. In this study we analyzed the same final WiggleZ galaxy sample as utilized by Blake et al. (2011c) for the measurements of BAOs in the galaxy clustering pattern. After cuts to maximize the contiguity of the observations, the sample contains 158,741 galaxies divided into six survey regions – the 9-hr, 11-hr, 15-hr, 22-hr, 1-hr and 3-hr regions. The survey selection function within each region was determined using the methods described by Blake et al. (2010).

2.2 The Gigaparsec WiggleZ simulation volume

We tested our methodology using data from the Gigaparsec WiggleZ (GiggleZ) N-body simulation (Poole et al. in preparation), a 2160³ particle dark matter simulation run in a $1h^{-1}$ Gpc box (with resulting particle mass $7.5 \times 10^9 h^{-1} M_\odot$). The cosmological parameters used for

the simulation initial conditions were $[\Omega_m, \Omega_b, n_s, h, \sigma_8] = [0.273, 0.0456, 0.96, 0.705, 0.812]$. Bound structures were identified using `Subfind` (Springel et al. 2001), which uses a friends-of-friends (FoF) scheme followed by a sub-structure analysis to identify bound overdensities within each FoF halo. We employed each halo’s maximum circular velocity V_{\max} as a proxy for mass, and used the centre-of-mass velocities for each halo when introducing redshift-space distortions.

Using the GiggleZ simulation halo catalogues we created one independent, complete realization of the set of six survey regions comprising the WiggleZ dataset. We constructed these mock catalogues by first selecting a subset of dark matter haloes spanning a small range of V_{\max} around 125 km/s, chosen to possess a similar clustering amplitude to the WiggleZ galaxies, and corresponding to halo masses around $10^{12} h^{-1} M_\odot$. We then subsampled these haloes using the survey selection function in each region to match the observed number of galaxies. The GiggleZ mock catalogues were used for testing the cosmological fits to the topological statistics for systematic errors, by checking for any significant deviation between the best-fitting parameters and the input cosmology of the simulation.

2.3 Lognormal density field catalogues

For each WiggleZ survey region we also constructed an ensemble of 400 lognormal realizations using the method described by Blake et al. (2011b). Lognormal realizations, which are Poisson-sampled from a density field built from a fiducial power spectrum model, are relatively cheap to generate and provide a reasonably accurate description of 2-point galaxy clustering for the linear and quasi-linear scales important for this analysis. Work is in progress to construct a larger set of N-body simulation mock catalogues for the WiggleZ survey, although this is a challenging computational problem because the typical dark matter haloes hosting the star-forming galaxies mapped by WiggleZ have mass $\sim 10^{12} h^{-1} M_\odot$, which (for example) is about ~ 20 times lower in mass than a Luminous Red Galaxy sample. The lognormal catalogues were subsampled using the survey selection function in each region to match the observed number of galaxies. They were used for determining the covariance matrix of the topological statistics at different density thresholds and the sparse-sampling correction, both described in more detail below.

2.4 Construction of the smoothed density fields

The cosmological density field of each dataset was constructed from the galaxy point distribution by smoothing with a Gaussian filter. In the smoothing process we must also correct for the effect of the varying survey selection function $W(\vec{x})$ with position \vec{x} . We introduce here a modification to the reconstruction method used in previous studies (e.g. Vogeley et al. 1994, James et al. 2009).

The previously existing methodology may be summarized as follows: i) Each galaxy within the data sample (D) is weighted with the value $1/W(\vec{x})$ and placed in a (padded) three-dimensional array using a nearest-grid-point binning; ii) these data are smoothed with a Gaussian (G) of standard deviation R ; iii) the systematically-lower density near

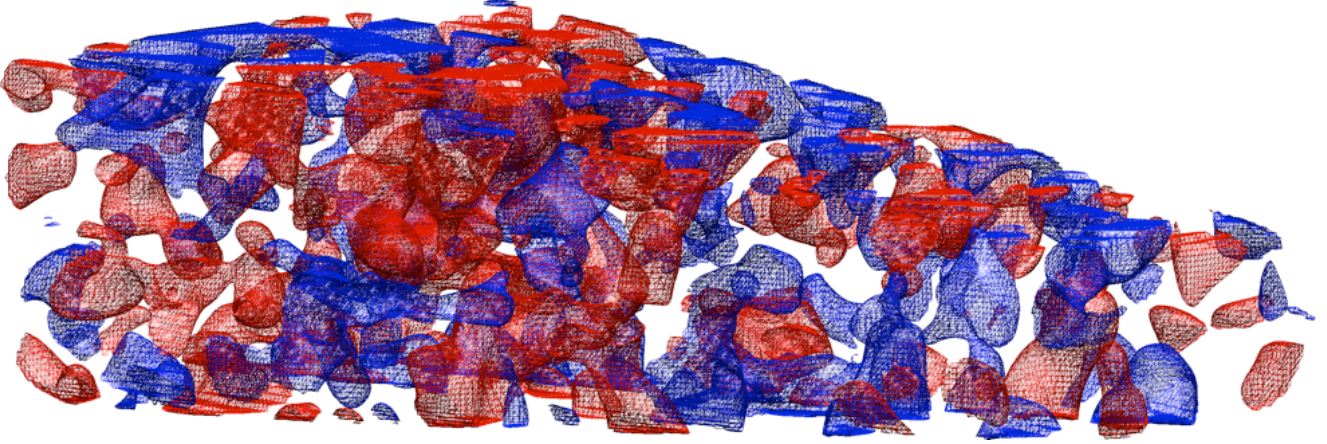


Figure 1. Density contours in the WiggleZ survey 15-hr region for a smoothing scale of $20 h^{-1}$ Mpc, extending from $z = 0.3$ (right of image) to $z = 0.9$, with the contouring chosen to excise the highest (red) and lowest (blue) 20% of volume within the field.

the survey boundaries induced by the smoothing is characterized by smoothing an array (C) that has constant value inside the survey volume and zero outside; iv) finally, the smoothed D field is taken in ratio with the smoothed C field, after which topology of structure within the resulting field can be studied. Formally, this process may be written:

$$F = [(D/W) \otimes G]/[C \otimes G], \quad (1)$$

where \otimes is used to denote convolution.

The alternative that we propose and implement here is: i) Do not weight the galaxies initially and instead smooth the galaxy counts in cells D as they are; ii) instead of creating a comparator field of constant value inside the survey region, weight the constant field by the selection function $C \times W(\vec{x})$; iii) smooth this weighted comparator field, which again is used in ratio with the smoothed data. In the notation described immediately above, this process may be summarized as:

$$F' = [D \otimes G]/[(C \times W) \otimes G]. \quad (2)$$

The motivation for the latter scheme is to apply the selection function to the data in a smoother and more global way, rather than locally at the site of each galaxy. In this sense, it is closer in spirit to the methodology used for correlation function estimation. These two schemes are identical in the limit that the selection function does not vary over the scale of the smoothing volume.

Figure 1 shows two isodensity surfaces within the reconstructed density field of the WiggleZ survey 15-hr region for the redshift range $0.3 < z < 0.9$, using a Gaussian smoothing scale $R = 20 h^{-1}$ Mpc. The isodensity values have been chosen so as to excise the highest and lowest density fifths of the field by volume, and the surfaces display the relative disconnectedness of structure that is expected for regions this far removed from the median density. The apparent uniformity of the topology of the structure with redshift relies on an accurate correction of the effects of the survey selection function, and the smoothness of the structures themselves is determined by the choice of filter.

3 MINKOWSKI FUNCTIONAL ANALYSIS OF GALAXY SURVEY DATA

3.1 Overview of Minkowski functional methodology

This work studies the topology of large-scale structure using the four Minkowski functionals of (the boundary surface of) excursion sets cut from the density field. An excursion set is constructed from the smoothed density field by choosing a critical density threshold (ρ_c); regions of density above this value are identified as being within the surface. The Minkowski functionals, which we computed by the algebraic means described in Appendix A, are identified geometrically with the enclosed volume, surface area, curvature and genus of the excursion set boundary surface. Hadwiger's theorem yields the result that these four statistics form a complete geometric description of the salient properties of the surface (see Chen 2004 for a recent review). Minkowski functionals have been explored in the context of cosmology by several authors for almost two decades (early analyses include Mecke et al. 1994, Kerscher et al. 1997, Schmalzing & Buchert 1997).

For convenience we remap the density threshold parameter ρ_c to a variable $\nu \in (-\infty, \infty)$ which is defined such that the fraction of volume V_{frac} enclosed by a given isodensity surface is

$$V_{\text{frac}}(\nu) = \frac{1}{\sqrt{2\pi}} \int_{\nu}^{\infty} e^{-\nu'^2/2} d\nu' = \frac{1}{2} \operatorname{erfc}\left(\frac{\nu}{\sqrt{2}}\right). \quad (3)$$

This step ensures that the first Minkowski functional – the enclosed volume – is identically an error function irrespective of the structure of the density field. Consequently it is the three remaining functionals, which we studied as a function of ν , that possess dispositive statistical power in the analysis.

This density transformation is equivalent to the Gaussianisation process of Weinberg (1992) employed in studies of reconstructing the linear-regime power spectrum (Neyrinck, Szapudi & Szalay 2011)

$$\nu \equiv \frac{f_G(\delta) - \bar{f}_G}{\sigma_{f_G}} \quad \text{where } f_G(\delta) \equiv \operatorname{erf}^{-1} \left[\int_{-\infty}^{\delta} f(\delta') d\delta' \right]. \quad (4)$$

This transformation maps the one-point density distribution $f(\delta)$ of the field to that of the normal distribution with mean

\bar{f}_G and standard deviation σ_{f_G} , preserving the ordering of regions from highest to lowest. It is also very similar to the lognormal transformation, given that the cosmological density field obeys a lognormal distribution even to the smallest scales we study in this work (Coles & Jones 1991, Taylor & Watts 2000, Watts & Taylor 2001).

The parameter ν indexes the surfaces drawn through the density field. The first two useful Minkowski functionals describe the area and curvature of these surfaces. There is less immediate geometric intuition for the final functional: the total connectedness, or genus statistic g . It is defined as the arithmetic difference between the total number of holes through the filamentary structure and its total number of disjoint components,

$$g = \text{number of holes} - \text{number of isolated regions} + 1. \quad (5)$$

The natural interpretation in the context of the cosmological density field is that the genus number measures how connected (when $g > 0$) or disjoint ($g < 0$) regions of a given density tend to be. Its numerical calculation often occurs indirectly via the computation of the total Gaussian curvature of the surface, a differential geometric technique introduced by Weinberg, Gott & Melott (1987). In this work we compute an equivalent statistic, the Euler characteristic [$= 4\pi(1 - g)$], as the final Minkowski functional.

3.2 Minkowski functionals of a Gaussian random field

The cosmological density field may be approximated, when filtered at certain scales, as a Gaussian random field. The theory of the statistics of excursion sets of such fields has been studied by many authors in contexts of cosmology and geometric statistics (Doroshkevich 1970; Adler 1981; Bardeen et al. 1983, 1986; Hamilton, Gott & Weinberg 1986; Tomita 1986; Gott, Weinberg & Melott 1987; Ryden 1988; Ryden et al. 1989; Matsubara 2003). For a three-dimensional Gaussian random field with power spectrum $P(k)$, smoothed by a Gaussian kernel $G(\vec{x}) = e^{-(\vec{x}\cdot\vec{x})/2R^2}$ with r.m.s. width R , the curves of the Minkowski functionals v_n , in terms of the density parameter ν , have a known analytical form,

$$v_n[\nu; P(k); R] = A_n[P(k); R] e^{-\nu^2/2} H_{n-1}(\nu). \quad (6)$$

Here, values of $n = \{0, 1, 2, 3\}$ correspond to the volume, surface area, mean surface curvature, and Euler characteristic, respectively, with H_n referring to the Hermite polynomial of degree n

$$H_n(\nu) = e^{\nu^2/2} \left(-\frac{d}{d\nu} \right)^n \{e^{-\nu^2/2}\}, \quad (7)$$

so that

$$H_0(\nu) = 1; H_1(\nu) = \nu; H_2(\nu) = \nu^2 - 1, \quad (8)$$

with the extension (Matsubara 2003)

$$H_{-1}(\nu) = \sqrt{\frac{\pi}{2}} e^{\nu^2/2} \operatorname{erfc} \left(\frac{\nu}{\sqrt{2}} \right). \quad (9)$$

The amplitude functional of the curves, A_n , is related to the power spectrum and smoothing scale in the following

manner:

$$A_n[P(k); R] = \frac{1}{(2\pi)^{(n+1)/2}} \frac{\omega_3}{\omega_{3-n} \omega_n} \left(\frac{\sigma_1^2[P(k); R]}{3\sigma_0^2[P(k); R]} \right)^{n/2}, \quad (10)$$

where $\omega_n = \pi^{n/2}/\Gamma(n/2 + 1)$ – in particular, $\omega_0 = 1$, $\omega_1 = 2$, $\omega_2 = \pi$ and $\omega_3 = 4\pi/3$ – and the generalized variance functionals are

$$\sigma_j^2[P(k); R] = \frac{1}{2\pi^2} \int k^{2j+2} P(k) e^{-k^2 R^2} dk. \quad (11)$$

We note that the dimensions of A_n , hence v_n , are $(\text{length})^{-n}$ – these equations describe the predicted Minkowski functionals per unit [length, area, volume] for $n = \{1, 2, 3\}$, matching the dimensions of the estimators described in the Appendix.

We now provide some intuition for the physical meaning of the ratio of power spectrum integrals that appears in equation 10, and for its dependence on the cosmological distance-scale adopted to analyze the survey data. Although in practice we always evaluate the exact integrals of equation 11, we note that the function $k^{2j+2} e^{-k^2 R^2}$, which weights the power spectrum in the integrals, peaks at wavenumber $k = \sqrt{1+j}/R$, and hence equation 11 approximately represents the ratio of two power spectrum amplitudes evaluated at scales $1/R$ and $\sqrt{2}/R$ (i.e. between two wavenumbers in a fixed ratio near $1/R$):

$$A_n \sim C_n \left[\frac{P(\sqrt{2}/R)}{P(1/R)} \right]^{n/2}, \quad (12)$$

where C_n is a constant. In other words, A_n intuitively depends on the effective slope of the power spectrum at the smoothing scale. Assuming a power-law power spectrum $P(k) \propto k^m$ as a concrete example, we can exactly solve the integrals to find that

$$A_n = C_n R^{-n} \left(\frac{3+m}{6} \right)^{n/2}. \quad (13)$$

Now suppose we change the distance-scale used to analyze the survey data, dilating all distances by a factor α . We follow the normal analysis practice for large-scale structure surveys, keeping the data measurements fixed and transferring the α dependence to the model. For fixed data there are two changes to model: (1) the smoothing scale R is effectively dilated to αR , and (2) there is an amplitude factor α^n corresponding to the dependence of the estimators in Appendix A on $(\text{length})^{-n}$. For the case of a power-law $P(k)$, for which $A_n \propto R^{-n}$, we can see that these two shifts cancel in equation 13 such that the model amplitudes have no dependence on the dilation scale α , hence cannot be used to constrain the distance scale, only the power-law slope m .

However, for a non-power-law $P(k)$, the model Minkowski functional amplitudes pick up a dependence on the distance scale α . In the intuitive form used in equation 12:

$$A_n \sim C_n \alpha^n \left[\frac{P(\sqrt{2}/\alpha R)}{P(1/\alpha R)} \right]^{n/2}. \quad (14)$$

The ‘curvature’ of the power spectrum $P(k)$ at the smoothing scale hence provides the ‘standard ruler’ which links the Minkowski functional amplitudes to the underlying distance scale.

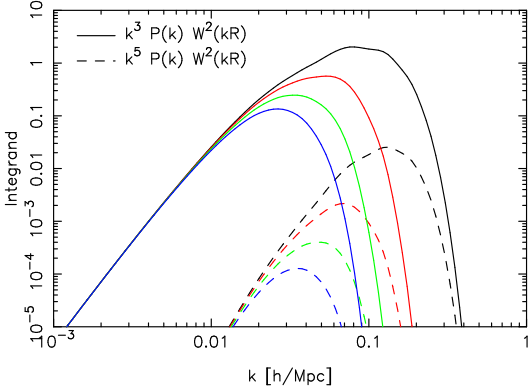


Figure 2. The integrands in k -space, given our fiducial power spectrum model, used in the determination of the amplitudes of the Minkowski functionals in equation 11, illustrating the range of scales to which these statistics are sensitive. The solid and dashed lines illustrate the integrands of σ_0^2 and σ_1^2 , respectively, and the four sets of curves, from top-right to bottom-left, correspond to the four Gaussian smoothing lengths $R = (10, 20, 30, 40) h^{-1}$ Mpc used in our analysis. Noting the logarithmic y -axis of the figure, we conclude that our measurements are principally sensitive to linear-regime scales $k < 0.15 h \text{ Mpc}^{-1}$.

In order to construct the model galaxy power spectrum that appears in equation 11, we started by generating a matter power spectrum using the **CAMB** software package (Lewis, Challinor & Lasenby 2000). We assumed the following values for the cosmological parameters: matter density $\Omega_m = 0.27$, Hubble parameter $h = 0.71$, physical baryon density $\Omega_b h^2 = 0.0226$, primordial spectral index $n_s = 0.96$ and normalization $\sigma_8 = 0.8$, inspired by CMB measurements from the *WMAP* satellite (Komatsu et al. 2011); we consider variations of this fiducial cosmological model in section 5 below, including the recent results reported by the *Planck* satellite (Planck collaboration 2013). We corrected the power spectrum for non-linear evolution using the ‘halofit’ prescription of Smith et al. (2003). This model power spectrum was subject to further modifications as described in section 3.3. We found that using the ‘halofit’, rather than linear, power spectrum to predict the Minkowski functional amplitudes was necessary to reproduce the results of the simulations.

Figure 2 displays the integrand of equation 11 for $j = (0, 1)$ as a function of $\ln k$, $k^{2j+3} P(k) e^{-k^2 R^2}$, for our fiducial power-spectrum model, illustrating the range of scales to which the topological statistics are sensitive for the smoothing lengths adopted in our analysis. We note that the information is dominated by linear-regime scales $k < 0.15 h \text{ Mpc}^{-1}$.

Figure 3 illustrates the unnormalized shapes of the $n = (1, 2, 3)$ Minkowski functionals for a Gaussian random field, with a view to providing some intuition for the statistics. We note the symmetry of these functions for positive and negative ν , such that the surfaces enclosing overdense and underdense regions possess similar topological properties. In the left-hand panel, the area of these surfaces can

be seen to vanish for the highest and lowest density values as expected, and to peak at average density. In the middle panel, the integrated mean curvature of the surfaces also tends to zero for the highest and lowest density regions, owing both to their vanishing area and to the fact that at such maxima the surfaces become spherical, and the sphere is the structure which minimizes integrated mean curvature. In the right-hand panel, the Euler characteristic also approaches zero for the highest and lowest peaks, given the diminishing number of regions in these limits. For large (moderate) departures from the mean density, the surfaces are preferentially disjoint (connected), corresponding to positive (negative) Euler characteristic, with a transition at $\nu = \pm 1$ owing to a cancellation between the number of isolated regions and number of holes specified in equation 5.

3.3 Modifications for non-linear processes

3.3.1 Galaxy biasing

An attractive property of the Minkowski functionals is that the density parameter ν undoes the process of any local, monotonic galaxy biasing scheme, such that in this model there is no effect of galaxy bias on the Minkowski functionals (Matsubara 2003), a result that remains true even in second-order perturbation theory for weakly non-Gaussian fields (Matsubara & Yokoyama 1996). This will not be the case for non-local or non-deterministic biasing prescriptions, which we do not consider here.

3.3.2 Redshift-space distortions

The observation of galaxies in redshift-space will impart anisotropic distortions on the power spectrum. On the large scales relevant to this analysis, the angle-averaged redshift-space power is given by

$$P(k) = b^2 P_{\delta\delta}(k) + \frac{2}{3} b f P_{\delta\theta}(k) + \frac{1}{5} f^2 P_{\theta\theta}(k) \quad (15)$$

(Kaiser 1987) where, in terms of the divergence of the peculiar velocity field θ , $P_{\delta\delta}(k)$, $P_{\delta\theta}(k)$ and $P_{\theta\theta}(k)$ are the isotropic density-density, density- θ and θ - θ power spectra, and f and b are the cosmic growth rate and galaxy linear bias factor, respectively. As discussed above, we produced the matter power spectrum for our fiducial cosmological parameter set using the ‘halofit’ model, $P_{\delta\delta} = P_{\text{halofit}}$. We then generated the velocity power spectra $P_{\delta\theta}$ and $P_{\theta\theta}$ using the fitting formulae in terms of $P_{\delta\delta}$, calibrated by N-body simulations, proposed by Jennings, Baugh & Pascoli (2011). We do not include small-scale velocity dispersion (‘fingers-of-god’) in our model. Our justification of the validity of this model is provided by the tests we carried out on the N-body simulation mock catalogues, described below. We specified fiducial values of f and b as the prediction of the Λ CDM growth rate in our fiducial model and the best-fit to the WiggleZ galaxy 2D power spectra (Blake et al. 2011a), noting that these choices could be varied without significant effect on our final results. Figure 4 overplots a measurement of the WiggleZ galaxy power spectrum (Blake et al. 2010), combining all survey regions, and our fiducial power spectrum model, illustrating that the model provides a good description of the data in the range $k < 0.3 h \text{ Mpc}^{-1}$

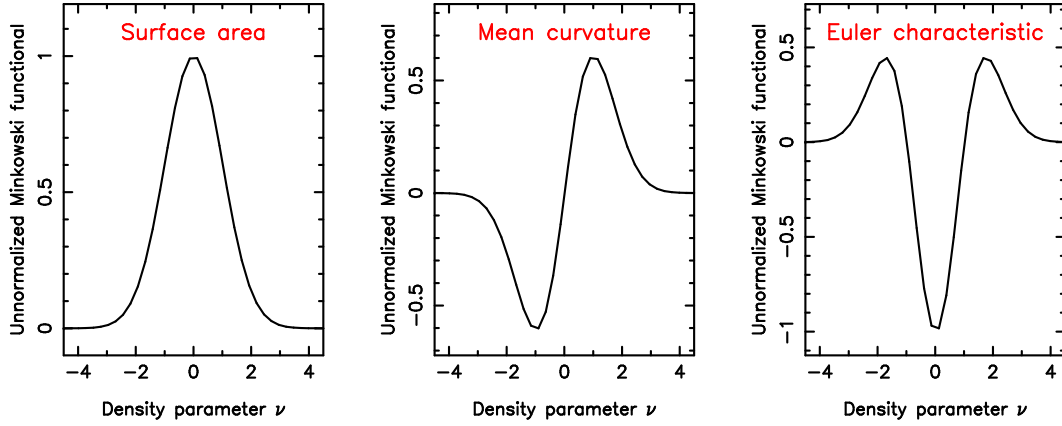


Figure 3. The unnormalized shapes of the $n = (1, 2, 3)$ Minkowski functionals for a Gaussian random field, $e^{-\nu^2/2} H_{n-1}(\nu)$.

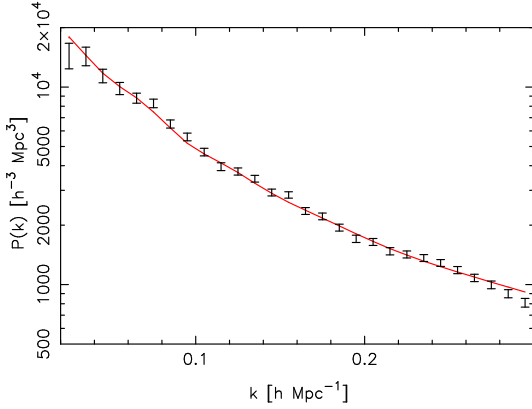


Figure 4. The WiggleZ galaxy power spectrum, combining measurements in the different survey regions, compared to the model defined in sections 3.2 and 3.3.2 which is used to produce the amplitudes of the Minkowski functionals. This model is a good description of the data for the range of scales relevant for the analysis.

($\chi^2 = 33.4$ for 27 degrees of freedom). As quantified further in section 4.3, this redshift-space distortion correction is negligible compared to the statistical errors in our measurements.

3.3.3 Non-linear evolution

Progress has been made in extending the expressions for the Minkowski functionals to weakly non-Gaussian fields, particularly those that depart from gaussianity as a result of primordial physics or non-linear gravitational evolution. We summarize here the model we used for the latter.

The perturbative approach to the study of non-linear gravitational evolution aims to describe higher-order statistics, such as the Minkowski functionals, in terms of the lower-order power spectrum. The Minkowski functionals are expressed in an Edgeworth-like expansion about the field variance σ_0 , with coefficients derived from the skewness parameters $S^{(i)}$ (Matsubara 1994, 2003). To leading order in

σ_0 this expression reads:

$$v_n(\nu) = A_n e^{-\nu^2/2} \left\{ H_{n-1}(\nu) + \sigma_0 \left[\frac{n}{3} (S^{(1)} - S^{(0)}) H_n(\nu) + \frac{n(n-1)}{6} (S^{(2)} - S^{(1)}) H_{n-2}(\nu) \right] + \mathcal{O}(\sigma_0^2) \right\}. \quad (16)$$

The skewness parameters are also derived from the power spectrum of the density field for each smoothing scale R :

$$S^{(0)}(R) = (2 + E)S_0^{11} - 3S_0^{02} + (1 - E)S_2^{11}, \quad (17)$$

$$S^{(1)}(R) = \frac{3}{2} \left[\frac{5 + 2E}{3} S_0^{13} - \frac{9 + E}{5} S_1^{22} - S_1^{04} + \frac{2(2 - E)}{3} S_2^{13} - \frac{1 - E}{5} S_3^{22} \right], \quad (18)$$

$$S^{(2)}(R) = 9 \left[\frac{3 + 2E}{15} S_0^{33} - \frac{1}{5} S_1^{24} - \frac{3 + 4E}{21} S_2^{33} + \frac{1}{5} S_3^{24} - \frac{2(1 - E)}{35} S_4^{33} \right], \quad (19)$$

where the cosmological factor $E \approx \frac{3}{7}$ and, with $l = kR$,

$$S_m^{\alpha\beta}(R) \equiv \frac{\sqrt{2\pi}}{\sigma_0^4} \left(\frac{\sigma_0}{\sigma_1 R} \right)^{\alpha+\beta-2} \times \int \frac{l_1^2}{2\pi^2 R^3} \frac{l_2^2}{2\pi^2 R^3} P\left(\frac{l_1}{R}\right) P\left(\frac{l_2}{R}\right) \times e^{-l_1^2 - l_2^2} l_1^{\alpha-3/2} l_2^{\beta-3/2} I_{m+1/2}(l_1 l_2) dl_1 dl_2 \quad (20)$$

where $I_m(x)$ is the modified Bessel function. Equation 16 specifies the final Minkowski functional model we used in our analysis, combined with the redshift-space galaxy power spectrum of equation 15. As quantified further in section 4.3, this non-linear evolution correction is negligible compared to the statistical errors in our measurements, partly because non-linear effects are absorbed by the volume fraction remapping of the density threshold parameter described by equation 3 (Matsubara 2003).

3.4 Differential Minkowski functionals

The Minkowski functionals, as introduced in the previous subsections and employed in cosmology to date, possess substantial covariance between density thresholds that has not

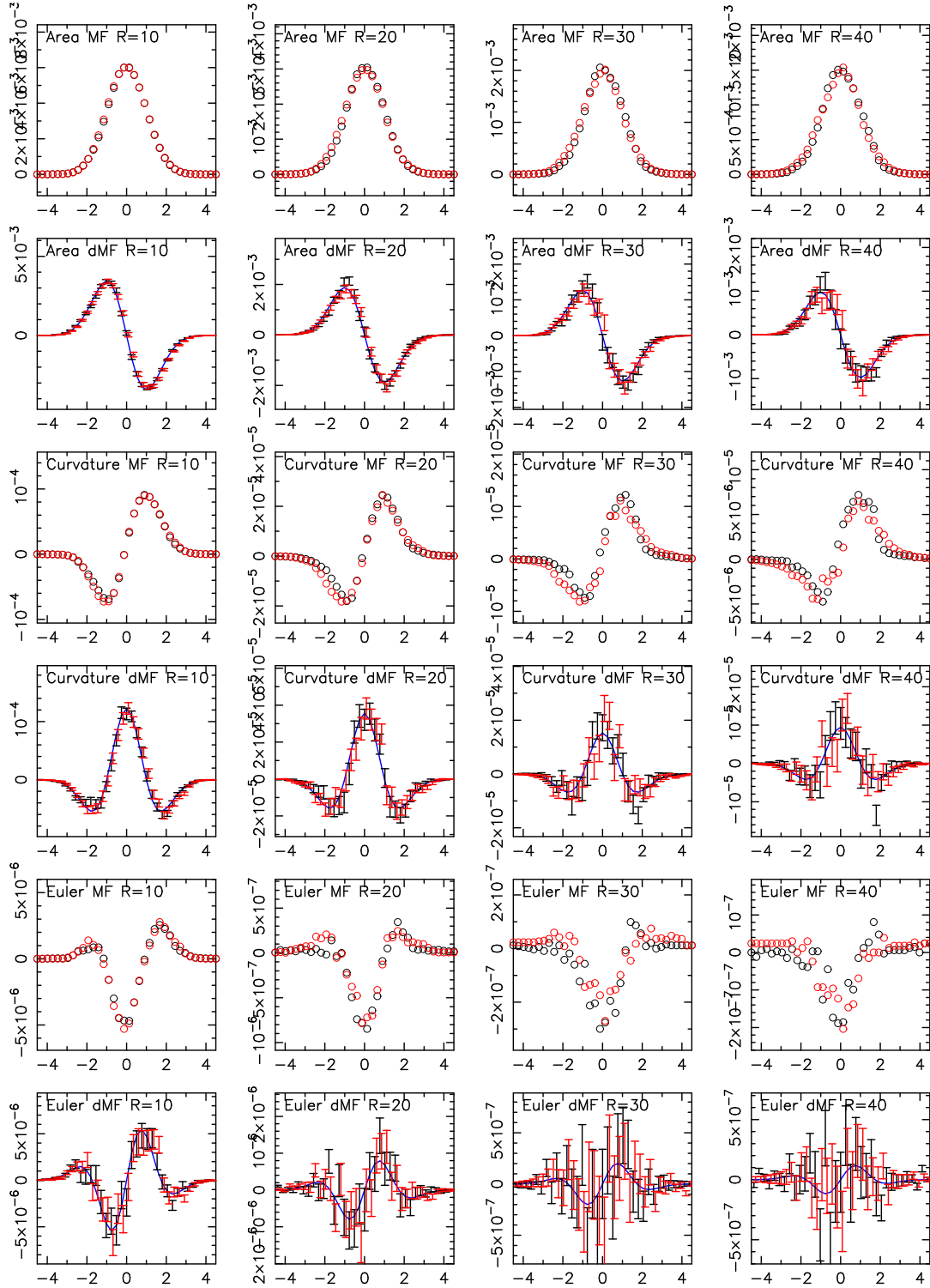


Figure 5. Minkowski functional measurements (open circles) and differential Minkowski function measurements (error bars) for the $z = 0.637$ narrow redshift slice of the WiggleZ 15-hr region for smoothing scales $R = 10, 20, 30$ and $40 h^{-1}$ Mpc. The black and red symbols represent the WiggleZ data and GiggZ simulation, respectively. The blue solid line displays the best-fitting model in each case, which is a good fit to the data, as discussed in the text. In each panel the x -axis represents the density variable ν and the y -axis plots the value of the (differential) Minkowski functional.

been fully detailed in previous work (although see the appendices of Choi et al. (2010) for recent progress in this endeavour). Recognising that a substantial source of this covariance is the use of integral excursion sets, such that each set is a subset of those that are excised subsequently, we advance the use of the *differential Minkowski functionals* of the disjoint part of each subsequent excursion set. We define the differential functionals using the algebraic difference between Minkowski functional measurements at adjacent density thresholds:

$$v'_n(\nu) = \frac{\Delta v_n(\nu)}{\Delta \nu}. \quad (21)$$

This is possible because the property of additivity, which the Minkowski functionals possess, ensures that for the incremental addition of δS to an excursion set S :

$$\begin{aligned} v_n(S \cup \delta S) &= v_n(S) + v_n(\delta S) - v_n(S \cap \delta S) \\ \Rightarrow v_n(\delta S) &= v_n(S \cup \delta S) - v_n(S), \end{aligned} \quad (22)$$

given that $v_n(S \cap \delta S)$ is the null set, since δS is disjoint to the previous surface S . Although the differential functionals contain no extra information compared to the integral versions, they result in a more closely-diagonal data covariance matrix (see section 4.2), which may therefore be estimated more robustly.

4 RESULTS

4.1 Measurement of topological statistics

We measured the three informative Minkowski functionals (surface area, curvature, Euler characteristic) of each WiggleZ survey region for four different Gaussian smoothing scales $R = 10, 20, 30,$ and $40 h^{-1}$ Mpc for 36 values of the density threshold parameter equally-spaced in the range $-4.5 < \nu < 4.5$, and converted each measurement to a differential Minkowski functional using a finite difference. We split the WiggleZ data into various redshift slices in the range $0.2 < z < 1$. First, we performed measurements in broad overlapping redshift ranges ($0.2 < z < 0.6, 0.4 < z < 0.8, 0.6 < z < 1$) in order to facilitate comparison with the BAO standard-ruler distances reported by Blake et al. (2011c). We also split each broad sample into three narrower, equal-volume redshift slices, such that a set of independent distance measurements could be constructed in six narrow redshift slices spanning $0.2 < z < 1$.

We repeated these measurements for the mock halo catalogues constructed from the N-body simulations. As described in section 2.2, we constructed one complete realization of all six WiggleZ regions for the central broad redshift range $0.4 < z < 0.8$, which matched the large-scale bias and selection function of the data sample. As above, we also split this sample into three narrower, equal-volume redshift slices spanning this range.

Figure 5 displays an example of the integral and differential Minkowski functional measurements, using the central narrow redshift slice ($z = 0.637$) of the range $0.4 < z < 0.8$ of the 15-hr survey region. The figure compares the WiggleZ survey measurement to that determined from the N-body simulation, and the best-fitting model. The WiggleZ and simulation results are in good agreement, and the model is a good fit to the data in all cases, as judged by the values

of the χ^2 statistic. For the 36 different combinations of 3 differential Minkowski functionals, 4 smoothing scales and 3 narrow redshift slices for the range $0.4 < z < 0.8$ of the 15-hr survey region, the average value of the best-fitting χ^2 is 34.6 for the WiggleZ data and 36.5 for the simulation data, both for 34 degrees of freedom.

4.2 Covariance matrices for differential Minkowski functionals

The covariance matrices of the differential Minkowski functional measurements in each region were determined by measuring these statistics for each of the ensemble of $N_{\log} = 400$ lognormal realizations. Writing the measurement at density threshold ν_i in the k th realization as $v_k(\nu_i)$, the covariance matrices were determined as

$$C(\nu_i, \nu_j) = \frac{1}{N_{\log} - 1} \sum_{k=1}^{N_{\log}} [v_k(\nu_i) - \bar{v}(\nu_i)] [v_k(\nu_j) - \bar{v}(\nu_j)], \quad (23)$$

where $\bar{v}(\nu_i) = \sum_{k=1}^{N_{\log}} v_k(\nu_i) / N_{\log}$. The corresponding correlation matrices $C(\nu_i, \nu_j) / \sqrt{C(\nu_i, \nu_i) C(\nu_j, \nu_j)}$ for each statistic are displayed in figure 6, comparing the integral and differential functionals for the measurements plotted in figure 5. This figure explicitly demonstrates that the covariance matrix of the differential form is more nearly diagonal than the integral form, as argued in section 3.4.

4.3 Correction for sampling systematics

The measurement of Minkowski functional statistics is systematically biased in the regime where the smoothing scale is comparable to the mean inter-galaxy separation (James 2012). Given the complexity of the WiggleZ survey selection functions there is no analytic description of this effect and we relied on an empirical correction using the lognormal realizations. We calculated this correction for each survey region and smoothing scale as the difference between the mean measured Minkowski functional of the lognormal realizations, and the Gaussian random-field model Minkowski functional corresponding to the underlying power spectrum used to generate the lognormal realizations (which is equivalent to the Minkowski functionals of the lognormal realization in the limit of high number density). We note that this additive correction, which is then applied to each Minkowski functional measurement from the survey data, is computed independently of any assumed cosmological model for either the volume of the real data or the non-linear corrections, but it does assume the fiducial power spectrum model used to generate the lognormal realizations; it is beyond the scope of this investigation to consider the model-dependence of this correction. The method is verified by its application to the mock catalogues generated from N-body simulations.

Figure 7 illustrates the relative magnitude of the sparse-sampling correction (in the upper row) for the most-affected smoothing scale, $R = 10 h^{-1}$ Mpc, again using the example of the central narrow redshift slice ($z = 0.637$) of the range $0.4 < z < 0.8$ of the 15-hr survey region. For the $10 h^{-1}$ Mpc smoothing scale the correction is comparable to the statistical error in the measurements; it is negligible for the other smoothing scales we considered. Figure 7 also displays

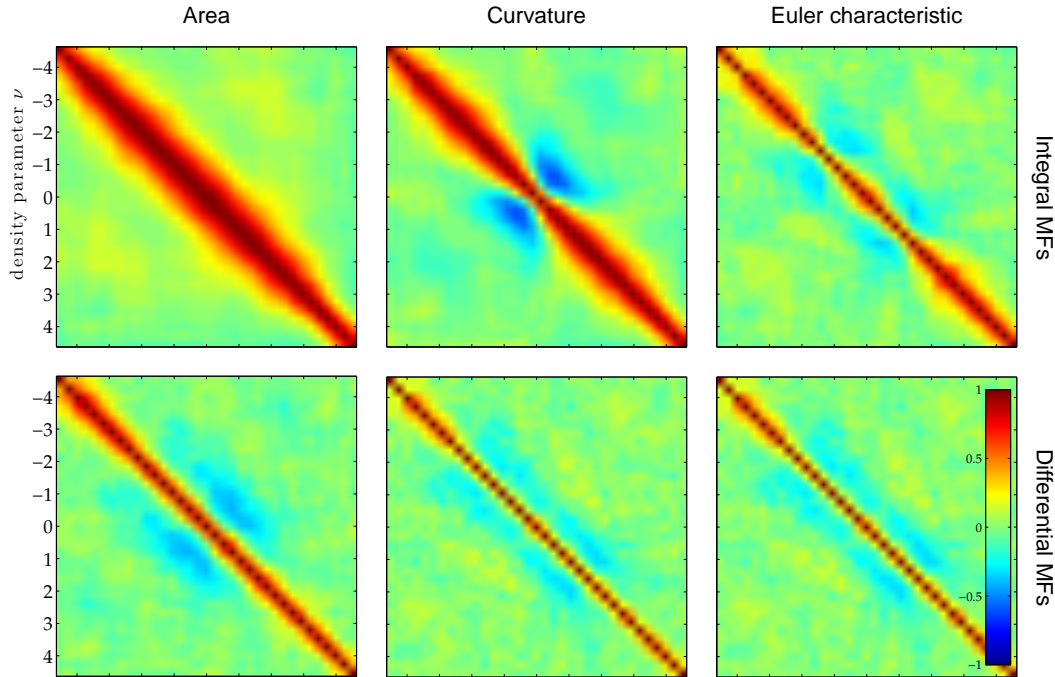


Figure 6. Correlation matrices for the three Minkowski functionals and their differential forms, generated from 400 realizations of a lognormal random field for the 15-hr survey region with the fiducial WiggleZ power spectrum, smoothed at a scale of $10 h^{-1}$ Mpc. The colour map has been scaled to the full range $[-1, 1]$, so that the off-diagonal regions give some indication of the noise present in the estimates.

the magnitude of the corrections implied by the non-linear evolution and RSD models described in section 3.3; these corrections are negligible in comparison with the statistical errors.

4.4 Measurements of Minkowski functional amplitudes

We fitted cosmological models to the Minkowski functional amplitudes, rather than the functions themselves, given that the amplitudes contain the cosmological distance-scale information. We fitted amplitudes A_i to the differential Minkowski functionals measured for each WiggleZ survey redshift slice and smoothing scale, using the covariance matrix determined from the lognormal realizations. The Minkowski functional model shapes, $v(\nu)$, were determined as the random Gaussian field models of section 3.2 with corrections for redshift-space distortions (section 3.3.2) and non-linear evolution (section 3.3.3). Due to the sparse-sampling correction already applied in section 4.3, no modelling of shot noise is required. In order to test for systematic errors, we repeated these amplitude fits for measurements from the N-body simulation catalogues.

Figure 8 displays an example of these amplitude fits, using the broad redshift range $0.4 < z < 0.8$ of the 15-hr WiggleZ survey region. There are hence 36 amplitude measurements (spanning 3 Minkowski functionals, 3 narrow redshift slices and 4 smoothing scales). For ease of presentation, the results are displayed divided by the predictions of the fiducial model. We note the good agreement between the amplitude measurements of the data and the mock cat-

alogues, and that the simulation results are consistent with the GiggieZ input cosmology.

4.5 Covariance matrix of amplitudes

The covariance matrix of the amplitude measurements, spanning different functionals and smoothing scales, was determined by applying the analysis pipeline described above to every lognormal realization, and deducing an amplitude covariance matrix using a relation analogous to equation 23. An example amplitude covariance matrix that results from this process is given in figure 9, which displays a 36×36 matrix corresponding to the measurements in figure 8. As expected, there are strong correlations between the amplitudes of different Minkowski functionals measured for the same redshift interval, and for the same functionals measured for different smoothing scales.

We note that building the covariance matrix from the lognormal realizations is a good approximation to the true data covariance. Considering the diagonal elements, the standard deviation of the amplitude fits to the lognormal realizations agreed closely with the standard deviation of the probability distribution obtained when the amplitudes are fitted to the real survey data.

5 COSMOLOGICAL MODEL FITS

5.1 Distance fits

Given the shape of the galaxy power spectrum at the relevant smoothing scales, the cosmological model described in

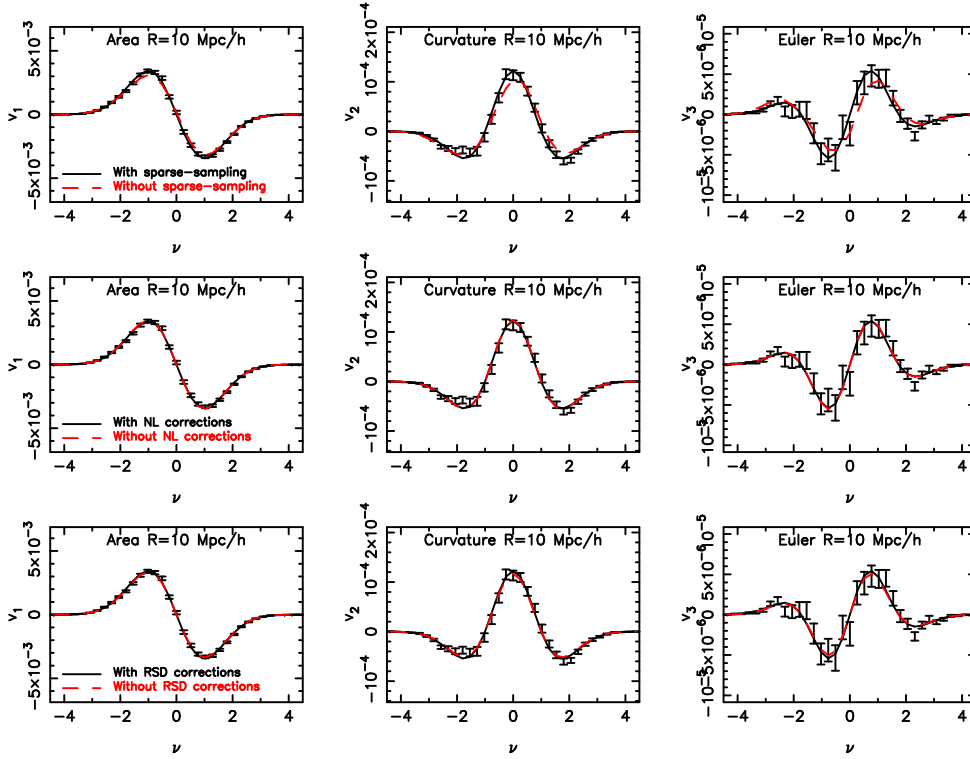


Figure 7. The magnitude of the non-gaussian corrections for sparse sampling (upper row), non-linear evolution (middle row) and redshift-space distortions (lower row), relative to the measured differential Minkowski functionals for the most-affected smoothing scale, $R = 10 h^{-1}$ Mpc. The panels display results for the $z = 0.637$ narrow redshift slice of the 15-hr survey region, with the black solid and red dashed line indicating the model with and without the application of the non-gaussian correction.

Table 1. Distance-scale fits to the topological statistics measured from the WiggleZ survey data and Giggles N-body simulation mock catalogues. The WiggleZ data is analyzed in a series of broad redshift ranges ($0.2 < z < 0.6$, $0.4 < z < 0.8$, $0.6 < z < 1$), which are also split into 3 narrow, equal-volume redshift subsamples. The mock catalogues were constructed for the range $0.4 < z < 0.8$. The last 4 columns of the table list the effective (volume-weighted) redshift z_{eff} of each measurement, the fit of $D_V/D_{V,\text{fid}}$ for fixed power spectrum shape, the value of the chi-squared statistic χ^2 for the best-fitting model and the number of degrees-of-freedom (‘dof’), and the fit of $D_V \Omega_m h^2$ marginalized over $\Omega_m h^2$, with D_V in units of Mpc. The fiducial distances, $D_{V,\text{fid}}$, are calculated at each effective redshift assuming a flat Λ CDM cosmological model with matter density $\Omega_m = 0.27$. A dataset of six independent distance measurements may be constructed using the results corresponding to slices (1, 2, 3) of the $0.2 < z < 0.6$ and $0.6 < z < 1$ redshift ranges.

Sample	Redshift range	slice	z_{eff}	$D_V/D_{V,\text{fid}}$	χ^2/dof	$D_V[\text{Mpc}] \Omega_m h^2/1000$
WiggleZ	$0.2 < z < 0.6$	joint	0.463	1.02 ± 0.04	53.1/35	0.213 ± 0.010
		1	0.304	1.16 ± 0.08	29.4/11	0.191 ± 0.012
		2	0.463	0.96 ± 0.07	11.3/11	0.205 ± 0.017
		3	0.559	0.97 ± 0.07	6.9/11	0.261 ± 0.020
WiggleZ	$0.4 < z < 0.8$	joint	0.637	0.96 ± 0.03	35.1/35	0.276 ± 0.009
		1	0.486	1.02 ± 0.05	9.7/11	0.250 ± 0.015
		2	0.637	0.92 ± 0.05	9.1/11	0.271 ± 0.017
		3	0.749	0.96 ± 0.05	13.6/11	0.319 ± 0.017
WiggleZ	$0.6 < z < 1$	joint	0.824	0.99 ± 0.02	41.7/35	0.328 ± 0.008
		1	0.680	1.00 ± 0.05	9.3/11	0.315 ± 0.016
		2	0.824	1.01 ± 0.04	14.7/11	0.362 ± 0.014
		3	0.944	0.98 ± 0.03	18.3/11	0.391 ± 0.014
GigglesZ	$0.4 < z < 0.8$	joint	0.637	0.99 ± 0.03	42.2/35	0.280 ± 0.009
		1	0.486	0.89 ± 0.06	7.5/11	0.222 ± 0.014
		2	0.637	1.05 ± 0.06	16.5/11	0.313 ± 0.018
		3	0.749	1.01 ± 0.05	13.4/11	0.340 ± 0.019

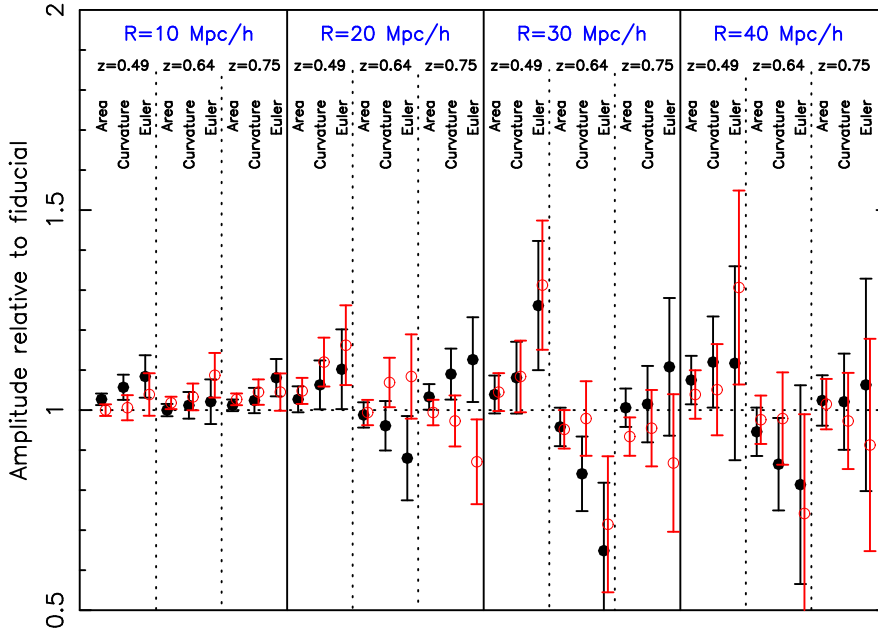


Figure 8. Amplitude measurements of each differential Minkowski functional for three narrow redshifts slices and four smoothing scales $R = (10, 20, 30, 40) h^{-1}$ Mpc for the broad redshift range $0.4 < z < 0.8$ of the 15-hr survey region. The solid (black) and open (red) circles represent the WigglyZ data and GigglyZ simulation, respectively. The amplitudes are divided by the prediction of the fiducial model defined in the text.

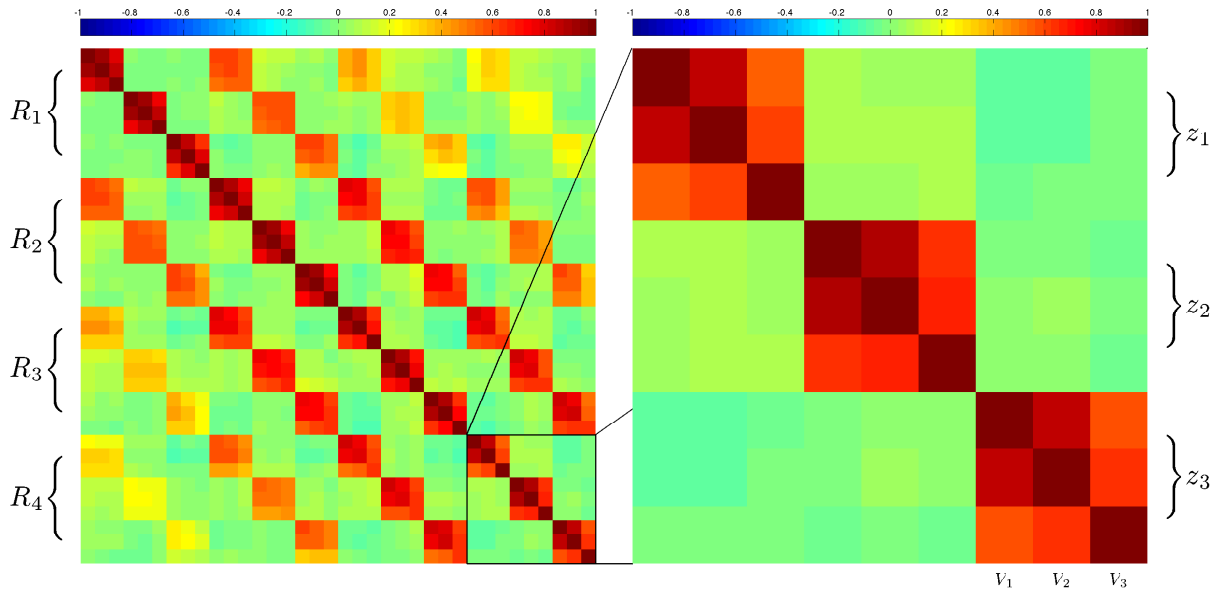


Figure 9. The covariance matrix of the amplitude measurements of the 36 sets of data encompassing combinations of the three Minkowski functionals v_i , three redshifts z_i and four smoothing scales R_i for the broad redshift range $0.4 < z < 0.8$ of the 15-hr survey region. The covariance is displayed as a correlation matrix relative to the colour bar at the top of the figure. The left-hand panel displays the full 36×36 correlation matrix, and the right-hand panel is a zoom-in of the lower-right 9×9 section corresponding to the largest smoothing length.

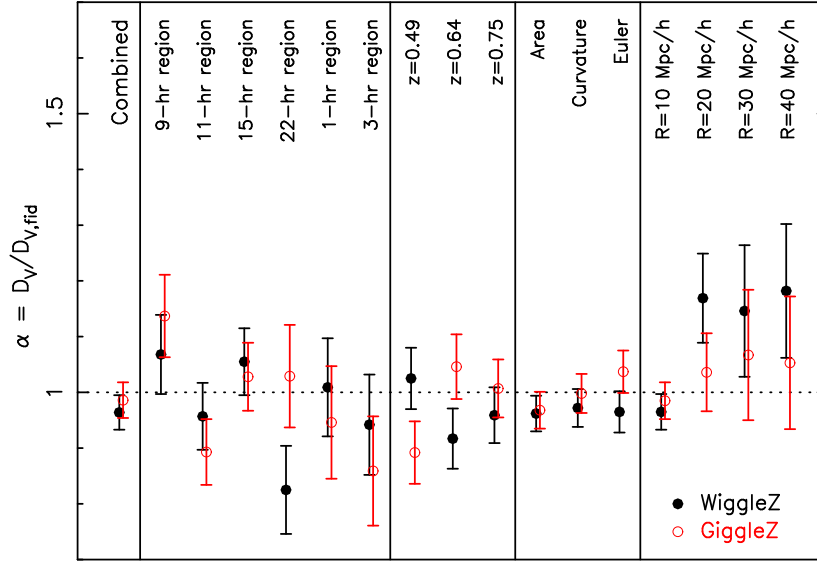


Figure 10. The results of distance-scale fits to the set of Minkowski functional amplitudes, using the WiggleZ data and simulations for the broad redshift range $0.4 < z < 0.8$. The far-left data point displays the measurement that results from combining the set of different survey regions, narrow redshift slices, Minkowski functionals and smoothing scales. The subsequent sections of the figure, from left to right, restrict the fits to individual regions, redshifts, functionals and scales. The solid (black) and open (red) circles show fits to the WiggleZ survey and GiggleZ simulation data, respectively. The fiducial cosmology used to calculate $D_{V, \text{fid}}$ is a flat Λ CDM model with matter density $\Omega_m = 0.27$.

sections 3.2 and 3.3 prescribes the amplitude of the topological statistics. The amplitude measurements were performed using our fiducial cosmological model, a flat Λ CDM model with matter density $\Omega_m = 0.27$, to determine the observed survey distance scale. If the true distance scale deviates from this fiducial cosmology, which we parameterize by a dilation in distances by a parameter α , then the model amplitudes must be adjusted in two ways:

- In the distorted model the dimensional Minkowski functional measurements would be scaled by a factor α^{-n} , where values of $n = \{1, 2, 3\}$ correspond to the surface area, mean surface curvature, and Euler characteristic, respectively. For an analysis keeping the data measurement fixed, the model amplitudes must therefore be scaled by α^n .

- In the distorted model the true smoothing scales R would have changed relative to the fiducial values $R_{\text{fid}} = (10, 20, 30, 40) h^{-1}$ Mpc used in the original computation. The distorted scales in the new cosmological model are given by $R = \alpha R_{\text{fid}}$.

The dilation scale α is related to the underlying cosmic distances by $\alpha = D_V(z)/D_{V, \text{fid}}(z)$, where $D_V(z)$ is the composite ‘angle-averaged’ distance that is measured using the baryon acoustic peak in the clustering monopole as a standard ruler (Eisenstein et al. 2005),

$$D_V(z) = \left[(1+z)^2 D_A(z)^2 \frac{cz}{H(z)} \right]^{1/3}. \quad (24)$$

where $D_A(z)$ is the angular diameter distance to the redshift slice and $H(z)$ is the Hubble expansion parameter. We can therefore fit the Minkowski functional amplitude measurements in each redshift slice for a single value of α , hence $D_V(z)$. We take the effective redshift z_{eff} of the measurement in each slice as the volume-weighted redshift of the pixels of the selection function which are used in the computation. We fitted the amplitudes after combining the Minkowski functional measurements in the different survey regions.

An example of these fitting results is displayed in figure 10, combining all survey regions for the $0.4 < z < 0.8$ redshift range, and comparing fits to the WiggleZ survey data and the GiggleZ N-body simulations. We show the results both combining all the different Minkowski functionals and smoothing scales, and dividing the signal into individual survey regions, narrow redshift slices, functionals and smoothing scales. We summarize the conclusions of figure 10 as follows:

- The distance-scale fits to the amplitudes measured from the N-body simulation mock catalogues produce results which are consistent with the input cosmology of the simulation, validating the method. The measurement of the distance-scale relative to the input cosmology of the simulation is $D_V/D_{V, \text{fid}} = 0.99 \pm 0.03$ and the value of the χ^2 statistic of the best-fitting model is 42.2 for 35 degrees of freedom.

- Each Minkowski functional carries roughly equal sen-

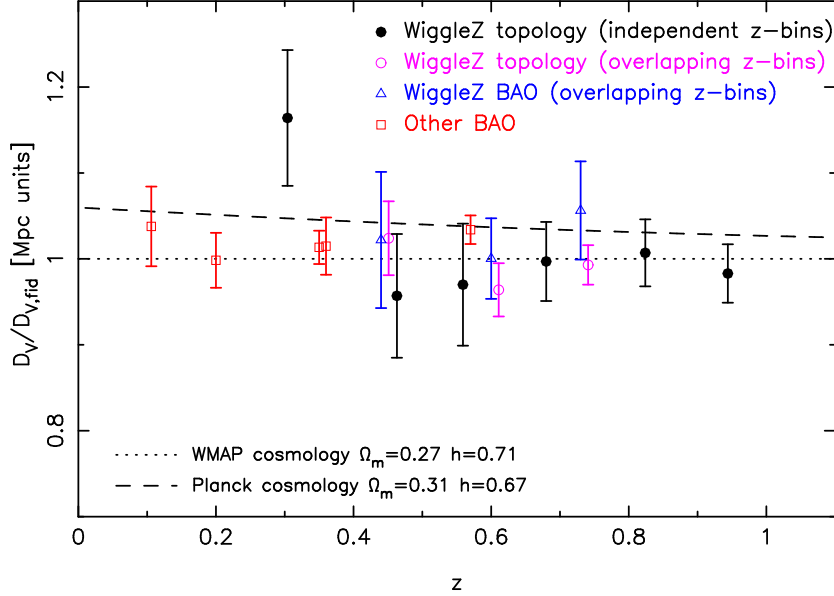


Figure 11. Comparison of distance-scale measurements from the standard-ruler fits to the WiggleZ topological statistics and recent BAO measurements from WiggleZ and other surveys. The WiggleZ topological measurements are shown with two independent binnings: the solid black circles are the results for six narrow, independent redshift slices spanning $0.2 < z < 1$, and the open black circles are the determinations in 3 broader, overlapping redshift ranges. These are chosen to coincide with the WiggleZ BAO analysis of Blake et al. (2011c), whose results are shown as the blue triangles. BAO measurements from other surveys are indicated as red squares, taken from Eisenstein et al. (2005), Percival et al. (2010), Beutler et al. (2011) and Anderson et al. (2012). The D_V measurements are plotted relative to the predictions of the *WMAP* fiducial cosmological model used in this paper; we also indicate on the figure as the dashed line the change relative to this model recently implied by the best fits to data from the *Planck* satellite (Planck collaboration, 2013). More details about the comparison of models and data are given in the text.

sitivity to the distance scale, with the area, curvature and Euler characteristic producing mutually-consistent distance measurements in the redshift range $0.4 < z < 0.8$ with accuracies of (3.1, 3.4, 3.6)%, respectively. The accuracy of the combined measurement is 2.9%, demonstrating that although these topological statistics are not independent, their combination does produce a slightly improved measurement compared to each individual statistic (in particular, an improvement of 20% compared to using the genus, i.e. Euler characteristic, alone).

- The fits are dominated by measurements at the smallest smoothing scale, $10 h^{-1}$ Mpc, which alone produces a 3.2% distance-scale determination. The precision resulting from larger smoothing lengths is lower, in the range 8 – 12% for $20 - 40 h^{-1}$ Mpc, due to the smaller effective number of independent data samples used to determine the topological statistics as the smoothing scale is increased.

5.2 Comparison with BAO distance measurements

Figure 11 compiles the overall set of distance-scale measurements from the fits to the WiggleZ topological statistics, and compares these with previous measurements of $D_V(z)$ using BAOs as a standard ruler. The black, solid circles are the

measurements from WiggleZ topology in six narrow, independent redshift slices spanning $0.2 < z < 1$, with accuracies in the range 3.3 – 7.7%. The black, open circles in figure 11 are the topological measurements in the broader redshift ranges ($0.2 < z < 0.6$, $0.4 < z < 0.8$, $0.6 < z < 1$), which are designed for comparison with the existing BAO distance measurements from the WiggleZ survey (Blake et al. 2011c). The two independent techniques for determining the distance scale produce consistent results, with the topological measurements yielding a higher accuracy by a factor of 2. However, the topological measurements also rely on more assumptions, in particular knowledge of the shape of the underlying redshift-space galaxy power spectrum, whereas the BAO technique relies more heavily on the single standard-ruler scale. The red squares in figure 11 are a compilation of other BAO distance-scale measurements from galaxy surveys in this redshift range (drawn from Beutler et al. 2011, Eisenstein et al. 2005, Percival et al. 2010 and Anderson et al. 2012).

In order to place the BAO measurements on figure 11 we combined the quoted values of $D_V(z)/r_s(z_d)$ with the latest *Planck* determination of the sound horizon at the baryon drag epoch, $r_s(z_d) = 147.4 \times 1.0275$ Mpc (Planck collaboration 2013), where the factor 1.0275 converts the exact determination of $r_s(z_d)$ to the approximation of the Eisenstein &

Hu (1998) fitting formula used by the BAO papers. We then divided the result (in Mpc) by the value of $D_V(z)$ in our fiducial cosmological model, for which $\Omega_m = 0.27$ and $h = 0.71$. We indicate as the dashed line in figure 11 the distances in Mpc relative to this fiducial model of the cosmological model favoured by *Planck*, $\Omega_m = 0.31$ and $h = 0.69$ (Planck collaboration 2013), which provides a somewhat better fit to the BAO dataset, particularly to measurements from the 6-degree Field Galaxy Survey (Beutler et al. 2011) and the Baryon Oscillation Spectroscopic Survey (Anderson et al. 2012).

The overall picture presented by these measurements is a consistent delineation of the cosmic distance-scale in the range $z < 1$. We note in particular that the WiggleZ topology measurements have extended this determination into the redshift range $0.8 < z < 1$, which was not accessible applying the BAO technique to the WiggleZ survey given that the effective shot-noise weighted cosmic volume it contains was insufficient to produce a significant detection of the baryon acoustic peak. The topological measurements, whose results are collected in table 1, do not necessitate a minimum observed volume.

5.3 Degeneracy with power spectrum shape

We now consider the significant degeneracy between the distance-scale measurements and the shape of the underlying galaxy power spectrum. For a pure CDM power spectrum, the matter transfer function at recombination can be expressed as a function of $q = k/\Omega_m h^2$ with k in units of Mpc^{-1} (Bardeen et al. 1986). Given that changing D_V corresponds to a scale distortion of $k \propto D_{V,\text{fid}}/D_V$, we recover that the measured statistics should depend on the combination $D_V \Omega_m h^2$ in this approximation, with D_V in units of Mpc.

This is illustrated by figure 12, which we generated by performing a joint fit of $\Omega_m h^2$ and $D_V/D_{V,\text{fid}}$ to the WiggleZ topological statistics, where the value of $\Omega_m h^2$ was used to produce the power spectrum model in each case (with the other cosmological parameters fixed at the values stated in section 3.2) and $D_V/D_{V,\text{fid}}$ was used to determine the volume distortion relative to the fiducial cosmology. As expected, the fits show that there is a significant degeneracy between these parameters. The dashed line in figure 12 indicates a set of constant values of $D_V \Omega_m h^2$, confirming that this quantity is indeed robustly constrained by the data, independently of $\Omega_m h^2$. In table 1 we list the best-fitting values of $D_V \Omega_m h^2$ for each data subsample, marginalized over $\Omega_m h^2$, which may be considered more ‘model-independent’ than the measurements of $D_V(z)$, which assume the fiducial cosmological parameter set. If we evaluate the χ^2 values of the ‘WMAP’ and ‘Planck’ (Ω_m, h) models defined above, (0.27, 0.71) and (0.31, 0.67), using the set of six independent measurements of $D_V \Omega_m h^2$ in narrow redshift slices from WiggleZ topology, we find that $\chi^2 = 6.2$ and 13.7, respectively, for 6 degrees of freedom. The corresponding ‘p-values’, indicating the probability of obtaining a χ^2 equal to these values or higher, are 0.40 and 0.033.

We note that the measurements of D_V using topological statistics are much more precise (by a factor of 3-4) than those which are obtained by fitting to the shape of the galaxy power spectrum data, distorting a template model

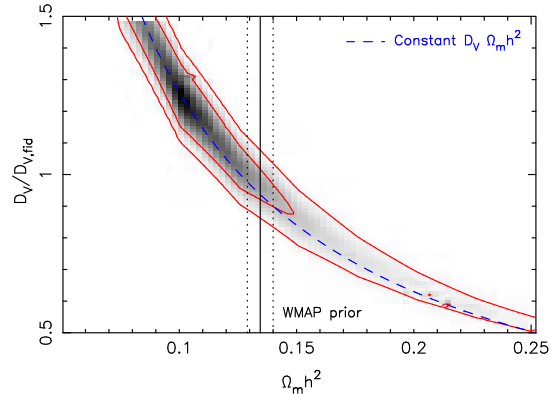


Figure 12. The joint probability distribution of $\Omega_m h^2$ and D_V that results from fits to the combined Minkowski functionals for the $0.4 < z < 0.8$ redshift range of the WiggleZ dataset. The blue dashed line displays the degeneracy direction of constant $D_V \Omega_m h^2$, which is well-constrained by the data. The vertical solid black line, together with the two vertical dotted lines, indicates the best-fit and $\pm 1\text{-}\sigma$ range of the measurement from *WMAP* (Komatsu et al. 2011), $\Omega_m h^2 = 0.1345 \pm 0.0055$.

by a scaling factor $\alpha = D_V/D_{V,\text{fid}}$ and marginalizing over a normalization factor (as performed for example in section 4.2 of Blake et al. 2011b). A possible reason for this is that the Minkowski functionals are independent of an overall normalization factor such as linear galaxy bias.

5.4 Validating the distance error

Given the impressive accuracy of the distance-scale measurements provided by these topological statistics, it is important to validate the plausibility of the errors. In this section we provide two supporting arguments.

First, we note that when the distance-scale fits are separately applied to each of the six individual WiggleZ survey regions that comprise our dataset, the scatter amongst the best-fitting values is approximately a factor $\sqrt{6}$ higher than the error in the joint measurement (as illustrated by the second section of figure 10), providing some approximate empirical verification of the measurement errors by division of the data into subsets. We also split the WiggleZ simulation catalogue into six realizations of the WiggleZ 15-hr region (as opposed to one realization of all six WiggleZ regions), and fitted a distance scale to each realization. We found that the scatter amongst the best fits was comparable to the error in the fit to the real 15-hr region dataset (indeed, the scatter in the simulation results was a little smaller, likely owing to the fact that the realizations are not truly independent, given that they have been carved from the same simulation).

Secondly, we demonstrate that the error in the fitted distance scale can be successfully estimated by propagating the error in the fitted Minkowski functional amplitudes. We take the example of the $z = 0.637$ narrow redshift slice, for which we obtain a 5% distance measurement (see table 1). For the surface area, mean surface curvature and

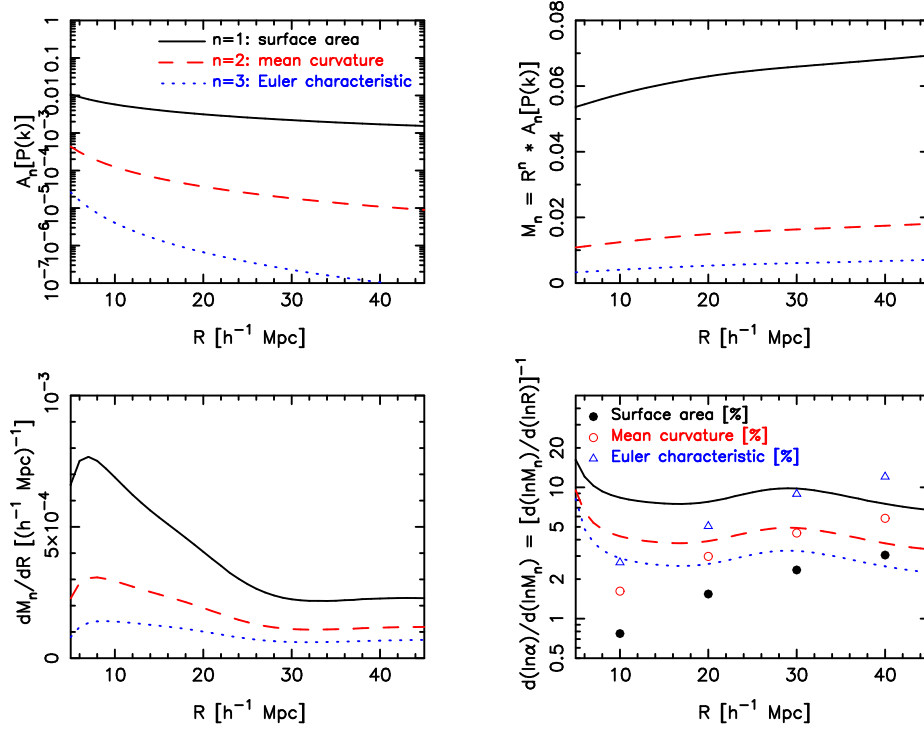


Figure 13. An illustration of the step-by-step propagation of the error in the Minkowski functional amplitudes A_n to the fitted distance scale α . In each panel, the black solid, red dashed and blue dotted lines represent functions describing the behaviour of the surface area, mean curvature and Euler characteristic, respectively. The top-left, top-right, bottom-left and bottom-right panels respectively display the dependence on smoothing scale $R = \alpha R_{\text{fid}}$ of the following quantities: the raw model amplitudes A_n , the combination $M_n = R^n A_n$ which is effectively constrained by the data, the rate-of-change dM_n/dR that gives the measurement the power to probe the distance scale, and the factor $d \ln \alpha / d \ln M_n$ which maps a fractional error in M_n to a fractional error in α . The measured errors in M_n are also shown in the bottom-right panel, for the three Minkowski functionals and four smoothing scales. The same y -axis range is used, with these quantities plotted as a percent error. More details and interpretation are provided in the text.

Euler characteristic, the errors in the measured amplitudes are (0.8, 1.6, 2.7)% for $R = 10 h^{-1}$ Mpc, (1.5, 3.0, 5.1)% for $R = 20 h^{-1}$ Mpc, (2.4, 4.5, 8.9)% for $R = 30 h^{-1}$ Mpc and (3.1, 5.8, 12.0)% for $R = 40 h^{-1}$ Mpc. As noted in section 4.5, these amplitude errors are in close agreement with the scatter of fits to lognormal realizations. Furthermore, the Euler characteristic errors agree well with the 4.2% measurement of the genus amplitude of a similar volume of SDSS Luminous Red Galaxies for a smoothing scale of $22 h^{-1}$ Mpc, recently presented by Choi et al. (2013).

Figure 13 illustrates the step-by-step propagation of the error in the Minkowski function amplitudes to the fitted distance scale α . The top-left panel displays the dependence of the amplitudes A_n of equation 10 on $R = \alpha R_{\text{fid}}$. This figure gives a falsely optimistic indication of the sensitivity of the measured amplitudes to α ; we must also consider the scaling of the measurements by α^n as the distance scale changes. This is encapsulated by the top-right panel, which shows the variation of $M_n = R^n A_n$ with R . These functions would be horizontal lines with no dependence on R for a power-law $P(k)$. The variation of M_n with α controls the propagation of errors from measured amplitudes to the distance scale, such that the fractional error in amplitude must be multi-

plied by a factor

$$\frac{d \ln \alpha}{d \ln M_n} = \left[\frac{R}{M_n} \frac{dM_n}{dR} \right]^{-1}, \quad (25)$$

to yield the fractional error in the distance scale. The functions dM_n/dR are plotted in the lower left-hand panel of figure 13, and the final factors $d \ln \alpha / d \ln M_n$ are shown in the lower right-hand panel. The accuracies of the measured amplitudes in the $z = 0.637$ narrow redshift slice are also displayed in this panel as a percentage, and it can be seen that multiplying these accuracies by the relevant factors traced by the lines successfully reproduces the $\sim 5\%$ distance-scale error. For example, error propagation for the measurements with $R = 10 h^{-1}$ Mpc smoothing scale predicts errors in α in the range 6.4 – 7.7% for the three Minkowski functionals; when combined with appropriate covariance and added to the (noisier) measurements for larger smoothing scales, the result is consistent with the final 5% distance error.

6 SUMMARY

We have presented the first measurements of the cosmic distance scale using the topology of the galaxy density field as

a standard cosmological ruler. If the shape of the underlying galaxy power spectrum is known, then the Minkowski functionals are prescribed via the statistics of the excursion sets of a Gaussian random field. Corrections due to non-Gaussian processes are small: the topological statistics are independent of any local, monotonic, non-linear galaxy bias and, for the smoothing scales considered in this analysis, are only weakly distorted by non-linear gravitational evolution and redshift-space distortions. As such, the topology of the density field in co-moving space is exactly conserved during linear evolution and, given the standard ruler provided by the known curvature of the underlying power spectrum, may be used to determine the same composite distance $D_V(z)$ that is probed using baryon acoustic oscillations.

We have applied these techniques to data from the WiggleZ Dark Energy Survey, implementing a number of methodological improvements compared to previous analyses:

- We utilized all Minkowski functionals in our analysis, whereas previous work has focused mainly on exploiting the genus statistic. Calculating the covariance between the topological statistics, we have shown that a combined analysis produces the most accurate distance measurements, and that the different statistics provide self-consistent results.
- We studied the differential, rather than integral, Minkowski functionals, in order to reduce the covariance between measurements at different density thresholds.
- We employed a series of lognormal realizations, with known topological statistics, to determine the correction to the Minkowski functionals from the sparse-sampling of the density field by the galaxy tracers. The complexity of the survey selection functions implies that this correction does not have an analytic form and must be determined numerically. The ensemble of lognormal realizations also provides an accurate covariance matrix of fitted Minkowski functional amplitudes, which we used to fit cosmological models.

We validated our methodology using mock catalogues sampled from an N-body simulation, which match both the selection function and large-scale clustering of the WiggleZ survey data, demonstrating that the fiducial cosmology of the simulation is recovered (within the statistical error of the analysis).

When analyzed in broad overlapping redshift ranges ($0.2 < z < 0.6$, $0.4 < z < 0.8$, $0.6 < z < 1$), the resulting distance-scale measurements from the WiggleZ survey have errors in the range 2.1 – 4.1%. These determinations agree with, and are almost twice as precise as, previous measurements from the same dataset using baryon acoustic oscillations as a standard ruler. We used arguments based on dividing the total dataset into sub-regions, and computing direct error propagation between the Minkowski functional amplitudes and distance scale, to increase confidence in the correctness of these errors.

The topological analysis requires more assumptions, since the full shape of the underlying power spectrum determines the Gaussian-field statistics. We describe this degeneracy by also providing measurements of the well-constrained combination $D_V \Omega_m h^2$, with errors in the range 2.4 – 4.7%. When analyzed in six narrow, independent redshift slices in the range $0.2 < z < 1$, the resulting measurements of $D_V(z)$ have errors in the range 3.3 – 7.7%, and agree with the ex-

isting set of BAO distance-scale measurements from other galaxy surveys, and with standard flat Λ CDM cosmological models.

We conclude that the utilization of the topological statistics of the galaxy density field is highly-merited as a complement to standard analyses based on 2-point statistics, and contains a different set of systematic errors. We have demonstrated that these topological measurements are capable of accurate determinations of the cosmic distance scale, as advocated by Park & Kim (2010) and Zunckel et al. (2011). In the future, topological statistics should also be useful for distinguishing between different models of gravity (Wang, Chen & Park 2012). Further work is required to model the non-linear effects of shot noise and redshift-space distortions on these statistics in a general fashion.

ACKNOWLEDGMENTS

We are very grateful for an extremely insightful and constructive referee report from David Weinberg, which greatly improved this paper. We also appreciated useful feedback on a draft of the paper from Tamara Davis, Karl Glazebrook, Matthew Colless and Fergus Simpson. JBJ is grateful for helpful discussions with Taka Matsubara. CB acknowledges the support of the Australian Research Council through the award of a Future Fellowship. JBJ was supported by the Sophie and Tycho Brahe Fellowship in Astrophysics jointly between UC Berkeley and the Dark Cosmology Centre, a position made possible by the Danish National Research Foundation. We acknowledge financial support from the Australian Research Council through Discovery Project grants DP0772084 and DP1093738 funding the position of GP. We are also grateful for support from the Centre for All-sky Astrophysics, an Australian Research Council Centre of Excellence funded by grant CE11000102.

Author contributions: All authors contributed to the development and writing of this paper. CB implemented the amplitude and cosmological fits, and most of the text and figures. BJ developed the tools for measuring the density field, the Minkowski functionals, covariance matrix and amplitudes, and contributed text (including the Appendix) and figures. GP generated the N-body simulation catalogues required for the analysis.

REFERENCES

- Adler, R.J., 1981, *The Geometry of Random Fields*, Chichester: Wiley
- Anderson, L., et al., 2012, MNRAS, 427, 3435
- Aragon-Calvo, M.A., van der Weygaert, R., Jones, B.J.T., 2010, MNRAS, 408, 2163
- Bardeen, J.M., Steinhardt, P.J., Turner, M.S., 1983, PRD, 28, 679
- Bardeen, J.M., Bond, J.R., Kaiser, N., Szalay, A.S., 1986, ApJ, 304, 15
- Barrow, J.D., Bhavsar, S.P., Sonoda, D.H., 1985, MNRAS, 216, 17
- Beutler, F., et al., 2011, MNRAS, 416, 3017
- Blake, C.A, Glazebrook, K., 2003, ApJ, 594, 665
- Blake, C.A., et al., 2010, MNRAS, 406, 803
- Blake, C.A., et al., 2011a, MNRAS, 415, 2876
- Blake, C.A., et al., 2011b, MNRAS, 415, 2892

- Blake, C.A., et al., 2011c, MNRAS, 418, 1707
 Busca, N.G., et al., 2013, A&A, 552, 96
 Chen, B., 2004, Geometriae Dedicata, 105, 107
 Choi, Y.-Y., Park, C., Kim, J., Gott, J.R., Weinberg, D.H., Vo-
 geley, M.S., Kim, S.S., 2010, ApJS, 190, 181
 Choi, Y.-Y., Kim, J., Rossi, G., Kim, S.S., Lee, J.-E., 2013, ApJS
 submitted
 Coles, P., Jones, B.J.T., 1991, MNRAS, 248, 1
 Coles, P., Plionis, M., 1991, MNRAS, 250, 75
 Coles, P., Davies, A.G., Pearson, R.C., 1996, MNRAS, 281, 1375
 Doroshkevich, A.G., 1970, Astrophysics, 6, 320
 Drinkwater, M.J., et al., 2010, MNRAS, 401, 1429
 Eisenstein, D.J., Hu, W., 1998, ApJ, 496, 605
 Eisenstein, D.J., Hu, W., Tegmark, M., 1998, ApJ, 504, 57
 Eisenstein, D.J., et al., 2005, ApJ, 633, 560
 Eisenstein, D.J., Seo, H.-J., White, M., 2007, ApJ, 664, 660
 Gott, J.R., Dickinson, M., Melott, A.L., 1986, ApJ, 306, 341
 Gott, J.R., Weinberg, D.H., Melott, A.L., 1987, ApJ, 319, 1
 Gott, J.R., Choi, Y.-Y., Park, C., Kim, J., 2009, ApJ, 695, 45
 Hamilton, A.J.S., Gott, J.R., Weinberg, D., 1986, ApJ, 309, 1
 Hu, W., Sugiyama, N., 1996, ApJ, 471, 542
 James, J.B., Colless, M., Lewis, G.F., Peacock, J.A., 2009, MN-
 RAS, 394, 454
 James, J.B., 2012, ApJ, 751, 40
 Jennings, E., Baugh, C.M., Pascoli, S., 2011, MNRAS, 410, 2081
 Kaiser, N., 1987, MNRAS, 227, 1
 Kerscher, M., et al., 1997, MNRAS, 284, 73
 Kim, J., Park, C., Rossi, G., Lee, S.M., Gott, J.R., 2011, JKAS,
 44, 6, 217
 Komatsu E., et al., 2011, ApJS, 192, 18
 Lavaux, G., Wandelt, B.D., 2012, ApJ, 754, 109
 Lewis, A., Challinor, A., Lasenby, A., 2000, ApJ, 538, 473
 Martinez, V.J., Jones, B.J.T., Dominquez-Tenreiro, R., van de
 Weygaert, R., 1990, ApJ, 357, 50
 Martinez, V.J., Paredes, S., Saar, E., 1993, MNRAS, 260, 365
 Matsubara, T., 1994, ApJL, 434, 43
 Matsubara, T., Yokoyama, J., 1996, ApJ, 463, 409
 Matsubara, T., 2003, ApJ, 584, 1
 Mecke, K.R., Buchert, T., Wagner, H., 1994, AAP, 288, 697
 Melott, A.L., Weinberg, D.H., Gott, J.R., 1988, ApJ, 328, 50
 Neyrinck, M.C., Szapudi, I., Szalay, A. S., 2011, ApJ, 731, 116
 Park, C., Kim, Y.-R., 2010, ApJ, 715, 185
 Peebles, P.J.E., Yu, J.T., 1970, ApJ, 162, 815
 Percival, W.J., et al., 2010, MNRAS, 401, 2148
 Planck collaboration, 2013, A&A submitted (arXiv:1303.5076)
 Poole, G.B., et al., in preparation
 Ryden, B.S., 1988, ApJL, 333, 41
 Ryden, B.S., et al., 1989, ApJ, 340, 647
 Schmalzing, J., Buchert, T., 1997, ApJL, 482, 1
 Seo, H.-J., Eisenstein, D.J., 2003, ApJ, 598, 720
 Seo, H.-J., Siegel, E.R., Eisenstein, D.J., White, M., 2008, ApJ,
 686, 13
 Smith, R.E., et al., 2003, MNRAS, 341, 1311
 Smith, R.E., Scoccimarro, R., Sheth, R., 2008, PhRvD, 77, 43525
 Springel, V., White, S., Tormen, G., Kauffmann, G., 2001, MN-
 RAS, 328, 726
 Sunyaev, R.A., Zeldovitch, Y.B., 1970, Ap&SS, 7, 3
 Taylor, A.N., Watts, P.I.R., 2000, MNRAS, 314, 92
 Tomita, H., 1986, Progress of Theoretical Physics, 75, 482
 Vo-geley, M.S., Park C., Geller, M.J., Huchra, J.P., Gott, J.R.,
 1994, ApJ, 420, 525
 Wang, X., Chen, X., Park, C., 2012, ApJ, 747, 48
 Watts, P.I.R., Taylor, A.N., 2001, MNRAS, 320, 139
 Weinberg, D.H., Gott, J.R., Melott, A.L., 1987, ApJ, 321, 2
 Weinberg, D.H., 1988, PASP, 100, 1373
 Weinberg, D.H., 1992, MNRAS, 254, 315
 Zunckel, C., Gott, J.R., Lunnan, R., 2011, MNRAS, 412, 1401

APPENDIX A: GÉOMÉTRIE SANS FRONTIÈRES, A MINKOWSKI FUNCTIONAL MEASUREMENT IMPLEMENTATION FOR SURVEY DATA

We describe an implementation of an algorithm to measure the Minkowski functionals at density thresholds $v_k(\nu)$ on data with non-periodic boundaries, as is the case for survey data that has been smoothed and corrected for selection effects. Similar enterprises have been discussed in works two decades past (e.g. Coles & Plionis 1991, Coles et al. 1996), though our approach is novel. Our routine blends the *Contour3D* algorithm of Weinberg (1988) with the integral geometric method for computing the functionals on smoothed fields, detailed by Schmalzing & Buchert (1997). Starting from a three-dimensional array, it sums the contribution to the four Minkowski functionals at each array node, where the contribution for each cell configuration about a node is retrieved from a pre-computed table. The notable distinction with respect to previous implementations is that the cell configurations now admit 3 values for a cell, corresponding to the cell being above the threshold, below the threshold and not in the survey region. This section describes how the look-up tables for contributions to the Minkowski functionals are computed, how the cell configurations are indexed and how the thresholding and summation is carried out. We validated our code using tests on a Gaussian random field generated from the *WiggleZ* survey galaxy power spectrum, including selection functions.

The theoretical necessity of an attentive study of boundaries can be understood from the Gauss-Bonnet theorem. Let \mathcal{M} be a two-dimensional surface separating regions above and below the threshold, and $\partial\mathcal{M}$ be the interface between this surface and regions outside the survey. Then the Euler characteristic χ , the fourth Minkowski functional, can be evaluated in relation to the Gaussian curvature K of the surface and the geodetic curvature k_g along the boundary:

$$\underbrace{\int_{\mathcal{M}} K dA}_{=4\pi(1-g)} + \int_{\partial\mathcal{M}} k_g ds = 2\pi\chi(\mathcal{M}). \quad (\text{A1})$$

The importance of the boundary term is that, when the surface is closed, the second integral vanishes and the Euler characteristic is interpreted geometrically as the genus of the surface ($\chi = 2 - 2g$). However, in the case of survey data it is not possible to assert that the surface is closed—one has no knowledge of the field outside the survey boundary. The integral geometric algorithm for computing the Minkowski functionals computes the left-hand side of this equation, incorporating the boundary term. This produces incorrect results for the surface area, curvature and Euler characteristic functionals, a simple demonstration of which is the limit where all of the survey region is above the density threshold: there are no interfaces between regions above and below the threshold, so the Minkowski functionals should have values $\{v_0, v_1, v_2, v_3\} = \{1, 0, 0, 0\}$; yet if the computation includes the boundary term, the latter three functionals will all be non-zero.

Inevitably, the boundary term must be subtracted, allowing the functionals to achieve their natural interpretations as volume, area, curvature and genus and to match

the theoretical formulae for these quantities that have been developed to date. This is achieved on-the-fly by requiring that the contributions to the Minkowski functionals at each node be altered in the presence of boundaries, which in turn mandates that this implementation operate on a ternary, rather than binary, threshold array.

A1 Computing Minkowski functionals with integral geometry

To discover how such a computation can be carried out, it is necessary to return to the fundamentals of Minkowski functional measurement on smoothed fields in cosmology, explicated most fully in the dissertation of Jens Schmalzing and summarized in his papers thereafter (Schmalzing & Buchert 1997)[†]. Crofton's 1868 formula for evaluating the length of a curve by counting its intersections with straight lines drawn through the plane can be extended to the surface in three dimensions. This casts the computation of these functionals as an integral over the intersections between the threshold surface and all possible hyperplanes. When the threshold surface is embedded in an array, however, the hyperplanes are those parallel to the lattice, so that the computation of the geometric properties of the surface is reduced to combinatorics of the point, line, surface and cube components of the cells within it.

In the absence of a survey boundary, the threshold surface defines a binary array of cells above and below the critical density. Identifying the cells above the threshold as those composing the volume, the total number of unique vertices N_0 , edges N_1 , faces N_2 and cubes N_3 within this volume, including those on its surface, are counted to give the Minkowski functionals (Schmalzing & Buchert 1997)

$$v_0 = \frac{a^3}{V} N_3 \quad (\text{A2})$$

$$v_1 = \frac{a^2}{V} \frac{2}{9} (N_2 - 3N_3) \quad (\text{A3})$$

$$v_2 = \frac{a}{V} \frac{2}{9} (N_1 - 2N_2 + 3N_3) \quad (\text{A4})$$

$$v_3 = \frac{1}{V} (N_0 - N_1 + N_2 - N_3) \quad (\text{A5})$$

Here, a is the physical length scale of an individual cell and V the physical volume of the field (i.e., $V = a^3 N$, where N is the number of cells in the array), so that the Minkowski functionals v_k are all expressed in physical units and as a fraction of the total volume of the field. The totals N_k are evaluated by summing the local contribution n_k at each node across the whole array.

This reduces the computation of the Minkowski functionals to a counting problem and remains valid even in the presence of survey boundaries. The crucial change when such a boundary is present is that the weight assigned to a cell component at the survey interface is reduced. To discover the manner in which this occurs, consider the case where the survey volume consists of a single cell of unit size,

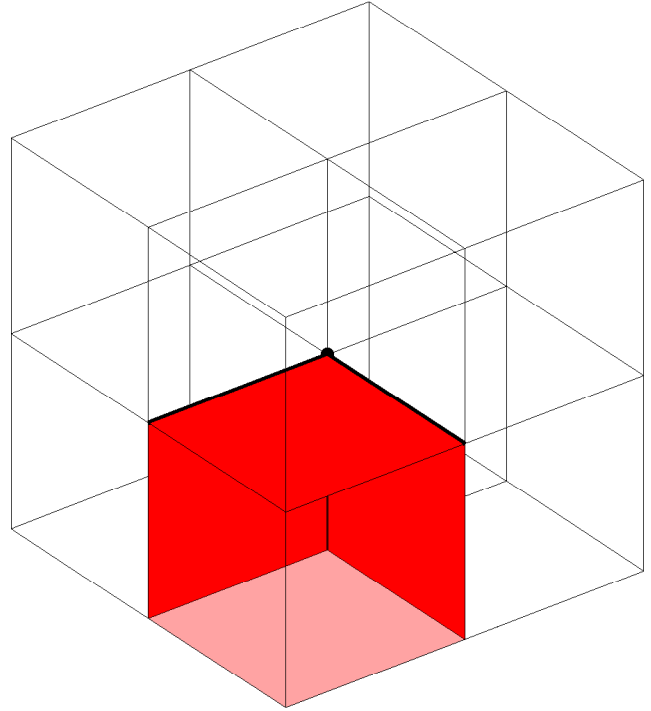


Figure A1. Visual description of the node indexing scheme used in this algorithm. Cell components are assigned to each array node (centre) as follows: one vertex (centre, large point), three edges (thickened lines), three faces (opaque shading) and one cube (shaded). This scheme ensures that every vertex, edge, face and cube within the array will be evaluated exactly once by looping over, or vectorized summation of, the array nodes.

above the threshold density, surrounded entirely by unit cells outside the survey volume. Once again, by geometric argument the Minkowski functionals of this survey region are $\{v_0, v_1, v_2, v_3\} = \{1, 0, 0, 0\}$, yet equations (A1) – (A4) will return

$$\{v_{0,1,2,3}\} = \left\{1, \frac{2}{9}(6-3), \frac{2}{9}(12-12+3), (8-12+6-3)\right\}.$$

This is resolved by reducing the contribution of a cell component to the count n_k from 1 to $1 - n_b/2^{3-k}$, where n_b is the number of cells outside the survey boundary with which the cell component is in contact. In this particular case, each vertex will now contribute $1 - \frac{7}{8}$, each edge $1 - \frac{3}{4}$ and each face $1 - \frac{1}{2}$. When the adjacent cells are not all outside the survey region, these weightings can take other integer multiples of $\frac{1}{8}$, $\frac{1}{4}$ and $\frac{1}{2}$ (between 0 and 1) for vertices, edges and faces respectively. It would not be uncharitable to characterize as incomplete our understanding of why this reweighting scheme succeeds. Some further clarifying examples will be provided in the sections below, after the numerical indexing scheme is described.

A2 Indexing scheme

Computing the number of cell components n_k comprising the thresholded region, without double counting, can be achieved by indexing each component uniquely to an array node. An arbitrary node within the array is surrounded by eight cells, of which one is assigned to that node; twelve

[†] This is an appropriate point for us to express our sadness at the tragic and untimely passing of Jens Schmalzing in 2005, whose work retains its great value to our field through its far-sighted understanding and uncompromising clarity of prose.

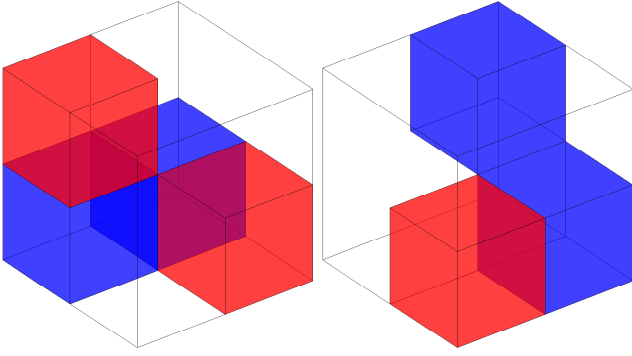


Figure A2. Examples of possible configurations, where red cells are above the threshold, empty cells below and blue cells outside the survey volume. The left configuration yields $n_{0,1,2,3} = \{\frac{6}{8}, \frac{3}{4} + 1 + \frac{2}{4}, 1, 0\}$ and the right configuration yields $n_{0,1,2,3} = \{\frac{6}{8}, 1 + \frac{3}{4} + \frac{3}{4}, 1 + 1 + \frac{1}{2}, 1\}$.

faces, of which three are assigned to that node; six edges, of which three are assigned to that node; and one vertex, the node itself. This configuration is demonstrated in figure A1. This means that each node can contribute $\{0, \frac{1}{8}, \frac{2}{8}, \dots, 1\}$ vertices, $\{0, \frac{1}{4}, \frac{1}{2}, \dots, 3\}$ edges, $\{0, \frac{1}{2}, 1, \dots, 3\}$ faces and $\{0, 1\}$ cubes to each of the totals n_k .

Algorithm 1 counts weighted contributions at node

Require: a 2^3 ternary array, A

$$\begin{aligned} n_0 &\leftarrow \mathbf{or}(A[:, :, :] = 1) \times (1 - \frac{1}{8}\Sigma(A[:, :, :] = 2)) \\ n_1 &\leftarrow \mathbf{or}(A[1, :, :] = 1) \times (1 - \frac{1}{4}\Sigma(A[1, :, :] = 2)) + \text{prms.} \\ n_2 &\leftarrow \mathbf{or}(A[1, 1, :] = 1) \times (1 - \frac{1}{2}\Sigma(A[1, 1, :] = 2)) + \text{prms.} \\ n_3 &\leftarrow (A[1, 1, 1] = 1) \end{aligned}$$

Given this specification, algorithm 1 evaluates the number of vertices, edges, face and cubes, with proper weightings for survey boundaries, at an individual node. In this notation, ‘=’ is used in the sense of logical evaluation, returning 1 when the condition is true, and returning a binary array of the same size as the object on the left-hand side; $\mathbf{or}(X)$ evaluates true when any member of the array slice X is true; and $\Sigma(X)$ is the sum over an array slice. Each of the three faces and edges indexed to the node are tested separately and these permutations have been suppressed in the expression for n_1 and n_2 .

Some examples may demonstrate this computation more clearly. Consider the arrangement shown in figure A1, assuming that the shaded cell is above the threshold and all others are both in the survey region and below the threshold. The contributions n_k at this node will be $\{1, 3, 3, 1\}$. Two trickier configurations (numbers 1380 and 3647 in the sequence of 3^8) are shown in figure A2.

A3 Cell configurations for Minkowski functional contributions

The algorithm examines the cell configuration at each node, counting the contribution from each cell component at-

tached to that node. We use an unbalanced[‡] ternary labelling system, where cells within the survey region and below the threshold are set to 0, those above the threshold to 1 and those outside the survey region to 2. There are, therefore, 3^8 possible configurations for the cell values about each node, which are enumerated by the following extension of the Weinberg (1988) scheme:

$$\begin{aligned} s_1 &= 3^3(1, 1, 1) + 3^2(1, 1, 2) + 3(1, 2, 2) + (1, 2, 1) \\ s_2 &= 3^3(2, 1, 1) + 3^2(2, 1, 2) + 3(2, 2, 2) + (2, 2, 1) \\ s &= 3^4 s_1 + s_2 + 1, \end{aligned} \quad (\text{A6})$$

where (i, j, k) is shorthand for the value of the corresponding cell within the 2^3 block surrounding the node. In the following we refer to this as a function \mathbf{idx} mapping a $2 \times 2 \times 2$ cell configuration to an index s . The cell $(1, 1, 1)$ is identified with shaded cube in figure A1.

Algorithm 2 Generate lookup table

```

for  $c = 0 \rightarrow 3^8 - 1$  do
   $n \leftarrow \text{base}_3(c)$  {i.e.,  $n$  is  $c$  in base 3, with 8 digits}
   $A \leftarrow \text{reshape}(n, [2, 2, 2])$  {pack digits into  $2^3$  array}
   $s \leftarrow \mathbf{idx}(A)$ 
   $[n_0(s), n_1(s), n_2(s), n_3(s)] \leftarrow \mathbf{counts}(A)$ 
end for

```

To speed up evaluation of the total counts N_k across the array, a lookup table is used. Algorithm 2 describes how this table is generated and indexed to node configurations, using the function \mathbf{counts} described in algorithm 1. Given a three-dimensional ternary array representing the thresholded density field, one determines the configuration at each node of the array using the function \mathbf{idx} and adds the contribution $n_k(s)$ from the table, summing these local contributions to give the total counts N_k that are the variables in equations (A1) – (A4).

[‡] The balanced scheme, where cells outside the survey are set to -1 , is conceptually attractive but cumbersome to compute.